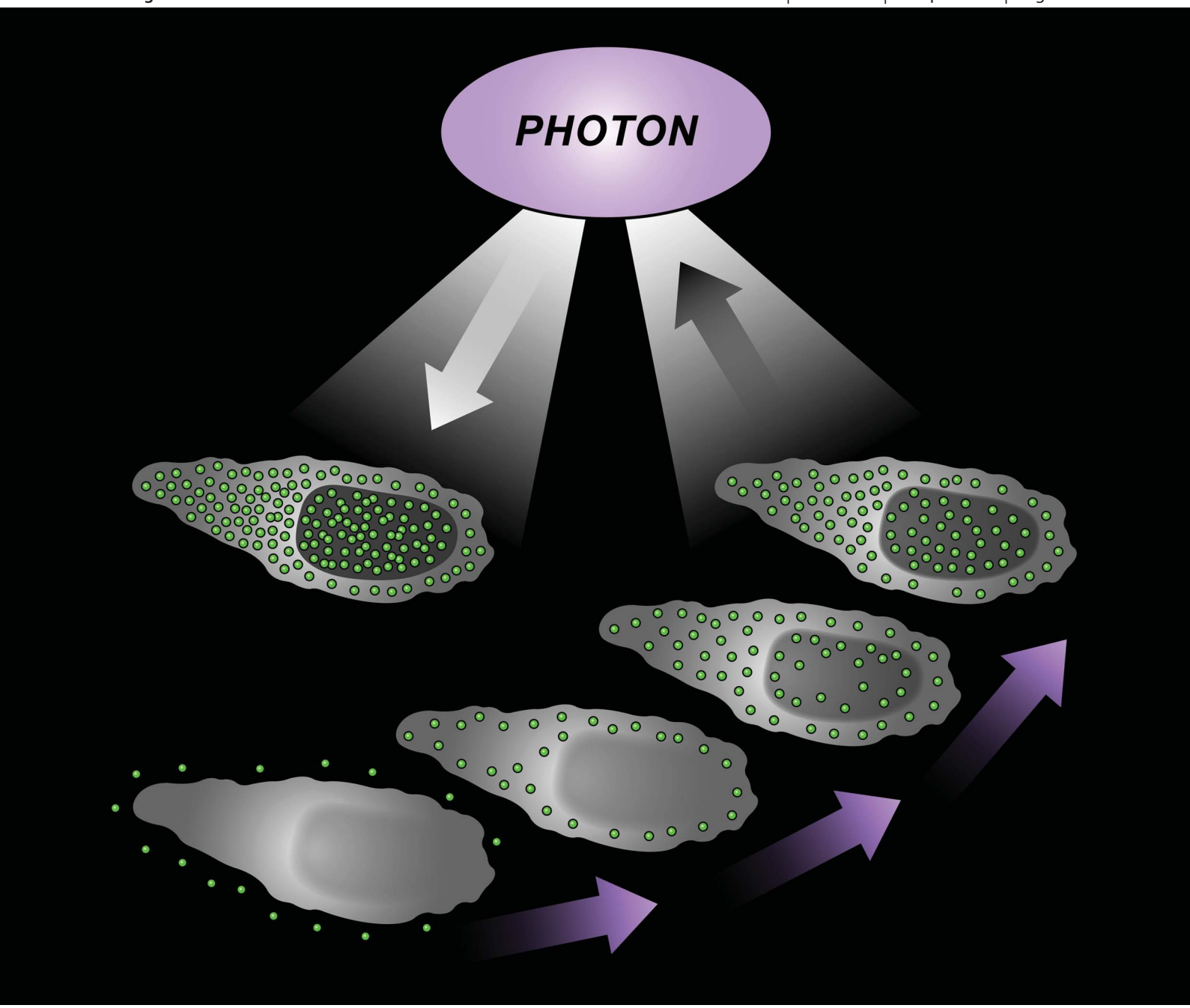
Nanoscale

www.rsc.org/nanoscale

Volume 4 | Number 9 | 28 April 2012 | Pages 2769–2984



ISSN 2040-3364

COVER ARTICLE

Xu *et al*.

Far-field photostable optical nanoscopy (PHOTON) for real-time super-resolution single-molecular imaging of signaling pathways of single live cells

COMMUNICATION

Sherman *et al*.

A zwitterion-DNA coating stabilizes nanoparticles against Mg^{2+} driven aggregation enabling attachment to DNA nanoassemblies

RSC Publishing

2040-3364(2012)4:9;1-H

Nanoscale

Dynamic Article Links

Cite this: *Nanoscale*, 2012, **4**, 2797

www.rsc.org/nanoscale

FEATURE ARTICLE

Far-field photostable optical nanoscopy (PHOTON) for real-time super-resolution single-molecular imaging of signaling pathways of single live cells†

Tao Huang, Lauren M. Browning and Xiao-Hong Nancy Xu*

Received 15th November 2011, Accepted 26th December 2011
DOI: 10.1039/c2nr11739h

Published on 04 January 2012 on http://pubs.rsc.org | doi:10.1039/C2NR11739H
Downloaded by Old Dominion University on 18 April 2012

Cellular signaling pathways play crucial roles in cellular functions and design of effective therapies. Unfortunately, study of cellular signaling pathways remains formidably challenging because sophisticated cascades are involved, and a few molecules are sufficient to trigger signaling responses of a single cell. Here we report the development of far-field **photo**stable-**o**ptical-**n**anoscopy (PHOTON) with photostable **s**ingle-**m**olecule-**n**anoparticle-**o**ptical-**bio**sensors (SMNOBS) for mapping dynamic cascades of apoptotic signaling pathways of single live cells in real-time at single-molecule (SM) and nanometer (nm) resolutions. We have quantitatively imaged single ligand molecules (tumor necrosis factor α, TNFα) and their binding kinetics with their receptors (TNFR1) on single live cells; tracked formation and internalization of their clusters and their initiation of intracellular signaling pathways in real-time; and studied apoptotic signaling dynamics and mechanisms of single live cells with sufficient temporal and spatial resolutions. This study provides new insights into complex real-time dynamic cascades and molecular mechanisms of apoptotic signaling pathways of single live cells. PHOTON provides superior imaging and sensing capabilities and SMNOBS offer unrivaled biocompatibility and photostability, which enable probing of signaling pathways of single live cells in real-time at SM and nm resolutions.

Department of Chemistry and Biochemistry, Old Dominion University, Norfolk, VA, 23529, USA. E-mail: xhxu@odu.edu; Web: www.odu.edu/sci/xu/xu.htm. Fax: +1 (757) 683-5698; Tel: +1 (757) 683-5698

† Electronic supplementary information (ESI) available. See DOI: 10.1039/c2nr11739h

Introduction

Binding of a few ligand molecules with their receptors on single live cells can initiate dynamic cascades of signal transduction, and alter cellular functions and cause diseases.[1–3] Currently,



Tao Huang

Dr Tao Huang received his BS degree in Chemical Physics from University of Science and Technology of China in 1998, and his PhD degree from University of North Carolina at Chapel Hill in 2003. He pursued his post-doctoral research at Brookhaven National Lab (2003–2005) and Old Dominion University (ODU) (2006–2008), and was promoted to a research scientist at ODU in 2009. His current research interests include synthesis and characterization of nanomaterials and their applications, ranging from developing nanoprobes for imaging of living organisms to design of high efficient solar cells, and single molecule detection (SMD).



Lauren M. Browning

Lauren M. Browning received her BS degree in biology from ODU in 2006. She is currently a PhD candidate in Biomedical Sciences under the direction of Dr Xu. She is the recipient of an NIH graduate research fellowship and an Old Dominion Fellowship. She has published several research papers, which demonstrate her wide range of research interests, including development of new tools for study of functions of single live cells in real-time, especially for probing of cellular signaling pathways, multidrug membrane transporters and differentiation of embryonic stem cells, as well as design of effective in vivo assays to study biocompatibility and toxicity of nanomaterials.

Published on 04 January 2012 on http://pubs.rsc.org | doi:10.1039/C2NR11739H
Downloaded by Old Dominion University on 18 April 2012

primary tools for study of such dynamic cascades are conventional ensemble non-real-time means, which cannot offer molecular and dynamic insights into cellular signaling pathways. Despite extensive studies over decades, few signaling pathways are fully understood and it remains formidably challenging to depict molecular mechanisms of signaling pathways in real-time.[4,5] Thus, it is vital to develop new tools for real-time molecular study of signaling pathways of single live cells with both temporal and spatial resolutions.

In this study, we have developed and used new imaging tools, PHOTON, to study molecular mechanisms and cascade dynamics of signaling pathways of single live cells in real-time at SM and nm resolutions. PHOTON uses single molecule silver nanoparticle (Ag NP) optical-biosensors (SMNOBS) as imaging probes. It consists of a standard dark-field optical microscope with a halogen-lamp illuminator and Multispectral Imaging System (MSIS) for spectral isolation of individual SMNOBS with 1 nm wavelength resolution.

Ag NPs possess distinct plasmonic optical properties and exceptionally high quantum yield of Rayleigh scattering that are orders of magnitude higher than fluorophores (*e.g.*, R6G).[6–10] They resist photobleaching and photoblinking.[11–13] These distinct optical properties enable us to image single Ag NPs as small as 2 nm in diameter using dark-field optical microscopy and spectroscopy (DFOMS).[10,11,13–19] We have used such small Ag NPs for sensing single biomarker molecules, probing ligand–receptor (L–R) interactions, and imaging single live cells and embryos in real-time at nm spatial and millisecond temporal resolutions.[10–19]

Unlike fluorescence-based microscopy and nanoscopy,[20,21] PHOTON detects Rayleigh scattering (but not fluorescence emission) of single Ag NPs with a white-light illuminator (no need for laser excitation sources). These approaches effectively overcome autofluorescence of live cells, photobleaching and phototoxicity of imaging probes, which are typical drawbacks directly associated with fluorescence imaging methods. Using intrinsic poly-dispersed localized surface plasmon resonance (LSPR) spectra of individual NPs, PHOTON effectively overcomes the need for switching on and off fluorophores widely used by fluorescence-based super-resolution microscopy.[12,20] Multiple cycles of switching on and off fluorophores are time consuming and cause phototoxicity toward living organisms.

Recently, we have demonstrated that PHOTON can map individual binding sites of single protein–ligand complexes, and achieve up to 1.2 nm spatial resolution.[12] This previous study validates super-resolution capabilities of PHOTON.

To shed new light on cellular signaling pathways and to demonstrate the proof-of-concept, in this study, we use PHOTON to investigate ligand (TNFα)-induced apoptotic signaling pathways of single live cells (L929) in real-time at SM and nm resolutions. Notably, apoptosis is an essential cellular process required for normal development. Defective apoptotic signaling pathways lead to numerous diseases.

TNFα is a pro-inflammatory cytokine that mediates a wide variety of cellular responses.[4,22,23] Numerous pathological conditions, including cancers, heart diseases, diabetes, and autoimmune diseases, overproduce TNFα, making TNFα an effective biomarker for diagnosis and treatment of a wide range of diseases.[1,24–26] Soluble TNFα (sTNFα, used in this study) binds with its receptors (TNFR1). Such binding reactions initiate dynamic cascades of cellular signaling and lead to cellular apoptosis.[5,27–29]

Despite extensive studies over decades, molecular mechanisms of TNFα–TNFR1 induced apoptotic signaling pathways, especially their dynamics, remain poorly understood.[29–31] It is unclear how many TNFα molecules are needed to bind with their receptors on each cell in order to initiate endocytosis and apoptosis, how long each step in dynamic cascades of signaling will take, and their dependence on the number of ligand and receptor molecules. It is entirely unknown how individual L–R complexes form clusters on the surface of single cells and whether single L–R complexes or/and their clusters internalize into the cells. Thus, it is crucial to address these vital questions, in order to fully understand cellular functions of TNFα for effective disease diagnosis and treatment.

Results and discussion

Synthesis and characterization of SMNOBS

Ag NPs were synthesized and characterized as described in the Experimental section. High-resolution TEM images of single NPs and histogram of their size distribution (Fig. 1A and B) show spherical NPs with average diameters of 2.6 ± 1.1 nm. Plasmonic images and LSPR spectra of single NPs (Fig. 1C and D) show blue and cyanic NPs with their peak wavelength (λ_{max}) and full-width-of-half-maximum (FWHM), λ_{max} (FWHM), ranging from 439 (55) to 496 (64) nm. The results indicate polydisperse plasmonic properties of single Ag NPs, and demonstrate that multiple individual NPs can be imaged and characterized simultaneously at single NP resolution. The results also underscore the importance of the study of plasmonic optical



Xiao-Hong Nancy Xu

Dr X. Nancy Xu received her BS degree in Physical Chemistry from Xiamen University, and her PhD in Chemistry from University of Mississippi. She pursued her postdoctoral research at UT-Austin and Ames Lab/Iowa State University, before joining ODU in 1998, and has held the position of Professor in Chemistry and Biochemistry since 2009. She is the AAAS fellow, and recipient of both Nano 50 Innovator and Technology awards for her pioneering work in single nanoparticle optical spectroscopy and nanobiosensors, and their applications in single live cell imaging. She directs NSF and NIH funded nanoscale interdisciplinary research programs, aiming to develop and apply cutting-edge bionanotechnologies and ultrasensitive methodologies to address most challenging questions in nano- and life sciences. Her research interests span from study of fundamental molecular mechanisms in living organisms to design of bio-inspired functional nanodevices.

This journal is © The Royal Society of Chemistry 2012

Published on 04 January 2012 on http://pubs.rsc.org | doi:10.1039/C2NR11739H
Downloaded by Old Dominion University on 18 April 2012

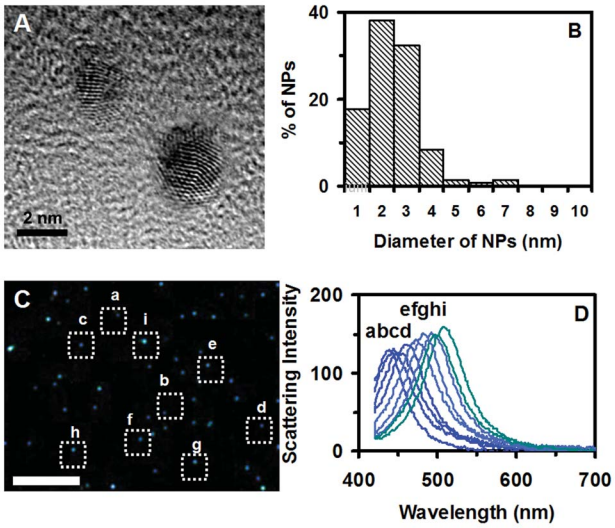


Fig. 1 Characterization of sizes and optical properties of single silver nanoparticles (Ag NPs): (A) HRTEM image of single Ag NPs and (B) histogram of size distribution of single NPs show single spherical NPs with average diameters of 2.6 ± 1.1 nm. (C) Dark-field optical image and (D) LSPR spectra of single NPs show plasmonic blue and cyanic NPs, as squared in (C), with λ_{max} (FWHM) at (a) 439 (55), (b) 442 (62), (c) 448 (64), (d) 460 (62), (e) 473 (64), (f) 482 (60), (g) 492 (64), (h) 496 (64), and (i) 508 (66) nm. The scale bars in (A) and (C) are 2 nm and 5 μm, respectively. The scale bar in (C) shows the distances between single NPs, but not the sizes of single NPs, due to the optical diffraction limit.

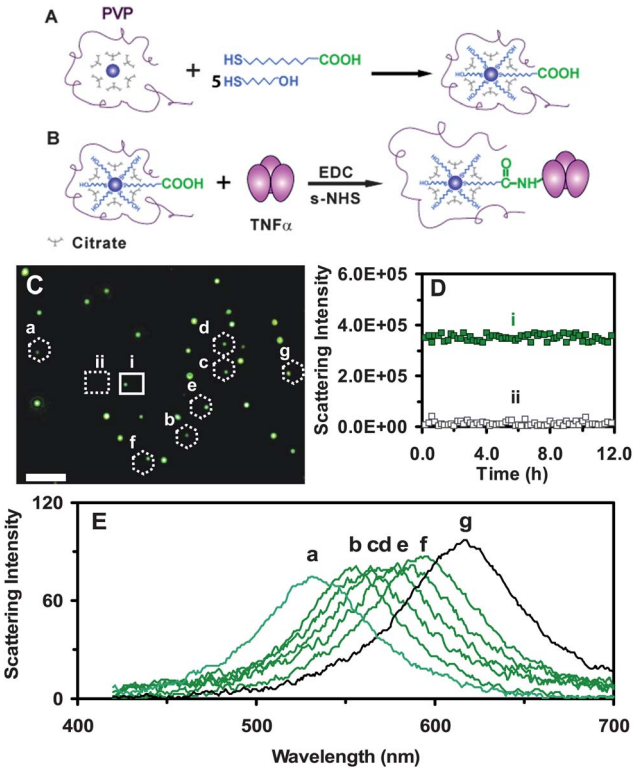


Fig. 2 Synthesis and characterization of SMNOBS. (A) Functionalization of Ag NPs with a monolayer of mixed MUA and MCH using the interaction of their thiol groups (–SH) with the surface of Ag NPs to prepare AgMMUA NPs with one MUA (carboxyl group) per NP, as characterized in Fig. S1 and S2†. (B) Synthesis of SMNOBS (AgMMUA–TNFα NPs) by linking the carboxyl group of the MUA (one per NP) on AgMMUA NPs with the amine group of TNFα *via* a peptide bond mediated by EDC and sulfo-NHS. (C) Dark-field optical images, (D) characterization of photostability, and (E) LSPR spectra of individual SMNOBS show single plasmonic green NPs with λ_{max} from 531 to 617 nm, and FWHM from 66 to 82 nm, and that SMNOBS resist photodecomposition and blinking. The scale bar in (C) is 5 μm, showing the distances among SMNOBS, but not their sizes, owing to the optical diffraction limit.

properties of individual NPs, rather than ensemble measurements of bulk NPs.

The Ag NPs were then functionalized with a monolayer of mixed MUA (11-mercaptoundecanoic acid) and MCH (6-mercapto-1-hexanol) *via* interactions of their –SH groups with the surface of Ag NPs to synthesize AgMMUA NPs (Fig. 2A). Some citrate molecules adsorbed onto the surface of Ag NPs were replaced by MUA and MCH *via* SN2 replacement reactions, owing to higher affinity of their –SH groups with the surface of Ag NPs than electrostatic interactions of citrates with the surface of Ag NPs.[11] NMR spectra of AgMMUA NPs (Fig. S1 in the ESI†) show a molar ratio of the surface functional molecules, citrate : MCH : MUA : PVP at 24 : 5 : 1 : 0.02, which indicates nearly absence of PVP. The cross-sectional (footprint) areas of one citrate, MCH and MUA molecule adsorbed onto the surface of NP are 0.514, 0.0458 and 0.0459 nm^2, as illustrated in Fig. S2† by a close-packing model, respectively.[11] Thus, the total footprint areas of 24 citrate, 5 MCH and one MUA molecules are 12.6 nm^2. The surface area of the NP (2.6 ± 1.1 nm in diameter) is 21.1 nm^2. Thus, much less than 48 citrates, 10 MCH and 2 MUA molecules are physically possible to attach onto one NP. Therefore, one MUA (one carboxyl group) is attached onto one NP.

Since only one carboxyl group (MUA) is available per NP, one carboxyl group can only conjugate with one amine group of TNFα *via* a peptide bond, no matter how many amine groups are available in a protein (TNFα) molecule. This simple approach limits one NP to be conjugated with one TNFα molecule *via* a peptide bond and enables synthesis of intrinsic SMNOBS (AgMMUA–TNFα NPs) with one TNFα molecule per NP (Fig. 2B).

The diameters of Ag, AgMMUA, and AgMMUA–TNFα NPs measured by dynamic light scattering (DLS) are 2.6 ± 1.1, 3.6 ± 1.6, and 9.8 ± 3.7 nm, respectively. The results further demonstrate one MUA molecule (length = 3.7 nm; diameter = 0.21 nm) per NP and one TNFα molecule (length = 6.1 nm; diameter = 5.4 nm; PBD: 2TNF) per NP (SMNOBS). If there were more than one MUA (or TNFα) molecule attached on the surface of the NP, each MUA (or TNFα) molecule would line up on the opposite side of the NP to create stable structures, owing to the charge repulsion of the molecules. The alignment would have led to the AgMMUA NPs and SMNOBS with much larger diameters than those measured by DLS.

Polydispersed and photostability of plasmonic properties of SMNOBS

Dark-field optical images of individual SMNOBS (Fig. 2C and E) show plasmonic green NPs and distinct λ_{max} of LSPR spectra, ranging from 531 to 617 nm, and FWHM from 66 to 82 nm. The

Published on 04 January 2012 on http://pubs.rsc.org | doi:10.1039/C2NR11739H
Downloaded by Old Dominion University on 18 April 2012

LSPR spectra of SMNOBS (Fig. 2) are red-shifted and broader, in comparison with those of Ag NPs in Fig. 1, which is attributed to their surface functional groups. The surface functional groups (MUA–TNFα, MCH) lead to chemical interface damping, decrease surface reflectivity, change surrounding environments and dielectric constants of Ag NPs, and increase the effective radii and aspect ratio of single NPs, which lower the LSPR energy and cause the red-shift of LSPR spectra.[6–8,32] The larger effective radii also lead to the longer dephasing time (T_2) and broader LSPR spectra with larger FWHM than those of the smaller NPs.[33]

The result in Fig. 2E demonstrates that none of individual SMNOBS has the same LSPR spectrum due to their high dependence on their sizes, shapes and surrounding environments.[8,9] The LSPR spectrum of each SMNOBS is effectively distinguished rapidly and simultaneously by MSIS, which enables individual NPs to serve as independent optical probes for multiplex imaging and sensing. In our recent study, we have demonstrated that such intrinsic poly-dispersed LSPR properties of SMNOBS of biotin molecules can serve as multi-spectral (color) imaging probes for sub-diffraction imaging; and we have validated spatial resolutions (up to 1.2 nm) of PHOTON.[12]

Scattering intensity of individual SMNOBS of TNFα remains constant over time under continuous irradiation of dark-field illumination (Fig. 2D), showing their superior photostability (non-photobleaching, non-photoblinking). Such superior photostability is essential to real-time tracking of binding, diffusion and clustering of single molecules and dynamic cascades of signaling pathways of single live cells for desired periods of time.

Binding affinity, specificity and dynamic ranges of SMNOBS

To determine the possible steric effects of NPs on the binding affinity of TNFα, we measured the binding constant (affinity) of SMNOBS with MAB in the PBS buffer by measuring the absorbance of SMNOBS (50 nM) incubated with their MAB (0, 10, 100, 200, and 500 nM) over time, respectively.[11,14] We used MAB of TNFα, instead of TNFR1, because TNFR1 is a membrane protein and subject to aggregation in the buffer, and MAB and TNFR1 share the same binding site of TNFα.[34]

As SMNOBS were incubated with MAB, absorbance of UV-vis absorption spectra of SMNOBS decreased over the incubation time, and their λ_{max} at 414 ± 2 nm remained essentially unchanged (Fig. S3A†), suggesting that SMNOBS bound with MAB and the bound SMNOBS did not contribute significantly to the absorption and scattering of unbound SMNOBS. The binding of SMNOBS with MAB led to the decrease of reflectivity and scattering quantum efficiency of NPs, and the increase of effective radii of NPs, which lower the absorbance and scattering of NPs.[6–8,32] The unchanged λ_{max} of absorption spectra of SMNOBS also shows that individual SMNOBS remain un-aggregated as they bind with MAB, and further demonstrates that NPs conjugated with TNFα (one TNFα per NP) do not lead to their aggregation. Otherwise, we would have observed the red-shift of the λ_{max}, if the aggregation of SMNOBS occurred.

The plot of the peak absorbance subtracted from baseline (ΔA) *versus* time in Fig. S3B† exhibits high linearity during the first 40 min of incubation time (Fig. S3C†), and then remains constant, suggesting that the binding of SMNOBS with MAB is a first-order reaction. Binding constant (4.1×10^6) and associated rate constant (1.7×10^2 M^{-1} s^{-1}) are calculated using the approaches as we described previously,[11,14] which agree well with those reported in the literature.[35] The results demonstrate that the TNFα conjugated with AgMMUA NPs retains its affinity and NPs do not create steric effects on their binding with MAB.

Plot of the maximum decreased peak absorbance (ΔA_{max} = absorbance of SMNOBS prior to their binding with MAB − absorbance of SMNOBS bound with MAB at equilibrium) *versus* concentration of MAB (Fig. S3D†) shows the linear calibration curve, indicating that ΔA_{max} is proportional to the concentration of MAB, and the dynamic range of SMNOBS is 0–500 nM. Blank control experiments were performed by incubating SMNOBS with BSA (500 nM) over time, which shows that the absorbance of SMNOBS remains essentially unchanged over time and the absorbance is independent of BSA concentration.

Design of PHOTON for real-time super-resolution SM imaging of single live cells

We then used SMNOBS as imaging probes and designed PHOTON to image TNFα-induced apoptotic signaling pathways of single live cells (L929) in real-time at SM and nm resolutions. As illustrated in Fig. 3, sequential dark-field optical images of (A) SMNOBS binding, diffusion and clustering on the surface of single live cells and (B) their internalization into the cell (5 μm in-depth inside the cells), are acquired over time using PHOTON. Simultaneously, sequential intracellular fluorescence images of Magic Red (assay used to monitor cellular apoptosis) are acquired using epi-fluorescence microscopy (C).

Magic Red caspases 3/7 assay can penetrate into live cells and determine apoptosis-related DEVDase enzyme activity in live cells.[36] Caspase-3 is the most important caspase of the executioner caspase group.[37] The Magic Red (cresyl violet fluorophore), (DEVD)2 caspase 3/7 fluorogenic substrate, is primarily targeted by the apoptotic protease cascade (caspases 3/7). When the Magic Red is di-substituted with two DEVD caspase-3/7 target sequences, it is non-fluorescent. As apoptosis occurs and progresses, caspase activity increases. The active form of caspases 3/7 in apoptotic cells causes the hydrolysis of the DEVD target sequences of the Magic Red, and converts it to the fluorescent form, which displays intense red fluorescence inside the cells.

As an example, dark-field optical images of SMNOBS bound with their receptors on single live cells are shown in Fig. 4A. LSPR spectra of the bound SMNOBS (L–R complexes) and scattering background of the cellular membrane (Fig. 4B) show that distinct plasmonic properties (green colors) of SMNOBS (Fig. 4C and D) enable them to be distinguished from the cells that appear white under a dark-field optical microscope. The scattering intensity of spot-(a) is ~4 times higher than that of spot-(b) (Fig. 4B), showing that spot-(a) consists of 4× more number of single L–R complexes located within the optical diffraction limit than spot-(b). Note that scattering intensity of the cluster of SMNOBS is proportional to their number.[6,8,10,12]

 This journal is © The Royal Society of Chemistry 2012

Published on 04 January 2012 on http://pubs.rsc.org | doi:10.1039/C2NR11739H
Downloaded by Old Dominion University on 18 April 2012

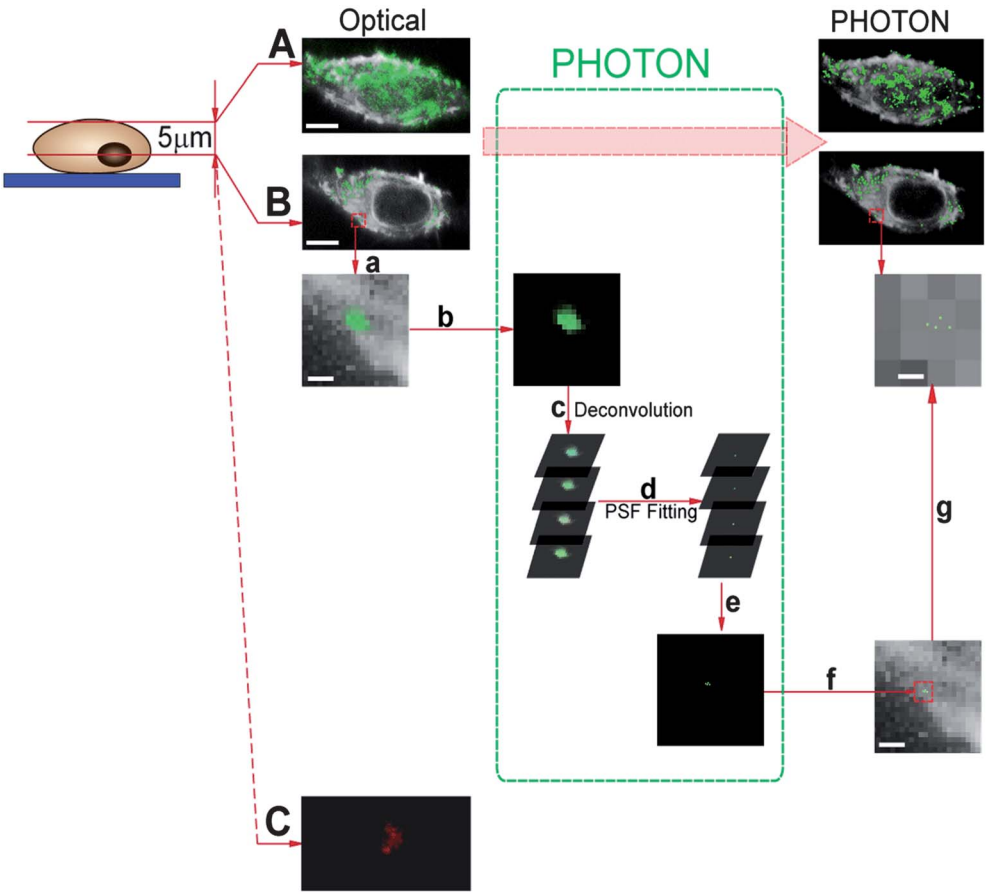


Fig. 3 Design of PHOTON for real-time super-resolution SM imaging of dynamics and mechanisms of apoptotic signaling pathways of single live cells. Dark-field optical imaging of: (A) single SMNOBS binding with TNFR1 to form single L–R complexes (bound SMNOBS) on the surface of single cells and (B) internalization of the clusters of single L–R complexes into the cell (5 μm in-depth from the cell surface): (a) zoom-in images of that squared in (B), as an example; (b) subtraction of (a) from scattering intensity of the cellular background spectrally; (c) images of the clusters of single L–R complexes are deconvoluted using LSPR spectra of single SMNOBS, (d) which are fitted by PSF to determine the number and locations of each complex; (e) distributions of multiple (20) measurements of (c and d) are fitted by 2D-Gaussian to determine the number and precise locations of bound SMNOBS at nm resolution; (f) scattering intensity of cellular background subtracted in (b) is added back to the super-resolution images in (e); and (g) assembly of (f) into super-resolution images of individual complexes on/in single live cells. (C) Fluorescence image of Magic Red (apoptosis assay) in single cells shows intense red fluorescence, indicating the apoptotic cell.

Stacks of such plasmonic images (image cubes) of single AgMMUA–TNFα–TNFR1 NPs (SMNOBS bound with TNFR1, L–R complexes) on and inside single live cells were acquired from 450 to 700 nm at each nm (1 nm spectral resolution) with 100 ms exposure time using MSIS. The broad LSPR spectra of clusters of the bound SMNOBS located within the optical diffraction limit in spots (a) and (b) were deconvoluted using the LSPR spectra of individual SMNOBS *via* the Cauchy–Lorentz model, as described by eqn (2)–(7) in the Experimental section.[12,38,39] The results (Fig. S4A†) show four deconvoluted LSPR spectra of individual SMNOBS in spot-(a), indicating that it contains four bound SMNOBS. In contrast, one LSPR spectrum (Fig. S6A†) was found for spot-(b), showing that one bound SMNOBS was present. The image of each SMNOBS with its deconvoluted spectrum was fitted by the point-spread-function (PSF) to determine their precise locations (centroids), as described by eqn (8) and (9) in the Experimental section (Fig. S4B and S6B†).[12]

The measurements were repeated 20 times, generating distributions of the centroids, which were fitted by 2D Gaussian to determine their precise locations with statistic accuracy, as described by eqn (8) and (9) in the Experimental section (Fig. S5 and S7†). Contour plots of the fittings (Fig. 4E and F) show four individual complexes with their precise locations for spot-(a), and one complex with its precise location for spot-(b). They are in contrast with their optical diffraction-limited images in Fig. 4C and D, which are unable to distinguish locations and number of SMNOBS.

Using the same approaches, the total number of L–R complexes in every spot (cluster) on the surface of every cell (Fig. 5A) and inside the cells (Fig. 5B) was determined over time. Images in Fig. 5 serve as examples to demonstrate super-resolution images of PHOTON in (b) and (d), which show precise locations and numbers of individual L–R complexes (bound SMNOBS), in contrast with their blurry optical-diffraction limit images in (a) and (c), which cannot distinguish individual bound SMNOBS. Around 10 individual cells similar to those in Fig. 5 were studied simultaneously over 900 min for each measurement, and 26 cells in total were studied for each experiment (Table S1†).

Published on 04 January 2012 on http://pubs.rsc.org | doi:10.1039/C2NR11739H
Downloaded by Old Dominion University on 18 April 2012

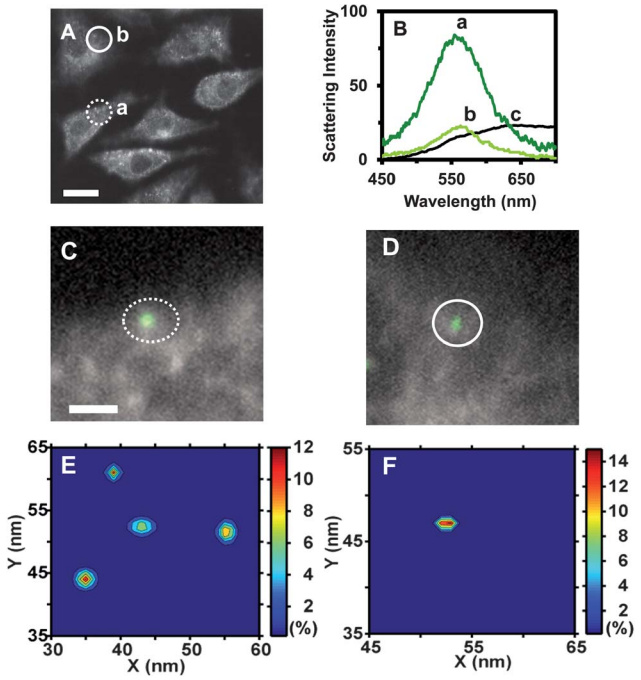


Fig. 4 Super-resolution SM imaging of single L–R complexes (bound SMNOBS) on single live cells using PHOTON. (A) Dark-field optical images of bound SMNOBS on single cells, as circled and labeled by (a) and (b), show distinctive plasmonic properties (green colors) of SMNOBS. (B): (a and b) LSPR spectra of the bound SMNOBS in spot (a) and (b) in (A), and (c) scattering background of the cell membrane. Nearly four times higher scattering intensity of bound SMNOBS in spot-(a) than spot-(b) is observed. (C and D) Zoom-in images of the spots circled in (A). (E and F) Contour plots of the number and precise locations (centroids) of individual L–R complexes show four L–R complexes and one complex in spots (a) and (b), respectively. The scale bars are 20 μm in (A) and 2 μm in (C–D).

Determination of spatial and temporal resolution of PHOTON

The spatial resolution of a far-field optical microscope in two dimensions has been described previously by Thompson *et al.*,[40] as shown in eqn (1):

$$\sigma = \sqrt{\frac{S^2}{N} + \frac{a^2}{12N} + \frac{8\pi S^4 b^2}{a^2 N^2}} \quad (1)$$

where σ is the uncertainty of the centroid (position) of an object; S is the standard deviation of PSF; a is the pixel size of the imaging detector; b is the standard deviation of background noise; and N is the number of collected photons.

The equation shows that far-field optical microscopy can achieve spatial resolution far beyond the optical diffraction limit, if sufficient amount of photons (N) from the object is collected.

We measured the number of photons (N) that each surface or internalized bound SMNOBS scattered and recorded by CCD camera, and used eqn (1) to calculate the spatial resolution of PHOTON.

The number of photons that individual bound SMNOBS scattered ranges from 9.1×10^3 to 1.3×10^4 with an average of $(1.1 \pm 0.1) \times 10^4$. The standard deviation (S) of PSF is (151 ± 4) nm; the standard deviation of the background noise (b) is (4.3 ± 0.3); and the pixel size of the CCD camera (a) is 100 nm. The spatial resolution (σ) of PHOTON calculated by eqn (1) shows that PHOTON has achieved spatial resolution up to 1.3 nm with averages of (1.5 ± 0.2) nm.

Such high spatial resolutions of PHOTON have also been validated experimentally in our previous study.[12] It is worth noting that the quantum efficiency (QE) of the CCD camera of 450–700 nm ranges from 0.58 to 0.46, respectively. Thus, PHOTON would potentially achieve sub nm (Å) spatial resolution with a more sensitive CCD camera (QE $\geq$ 0.8).

The temporal resolution of PHOTON relies upon the exposure time at each given wavelength to gain sufficient S/N ratios of single SMNOBS, while the observational resolution depends upon the spectral resolution, wavelength range and exposure time. For 1 nm spectral resolution with 250 nm wavelength range (450–700 nm) and 100 ms exposure time at each wavelength, it takes 25 s to obtain 1,447,680 spectra of each pixel of the full-frame image (1392×1040) for imaging of single SMNOBS bound with TNFR1 on/in single live cells at 1.3 nm spatial resolution. Thus, the temporal resolution is 100 ms and observation resolution is 25 s.

Notably, single SMNOBS can be detected with 5 ms exposure time using the MSIS. The wavelength ranges of single NPs could be narrowed to $\lambda_{max} \pm 5$ nm (10 nm within λ_{max} of LSPR spectra of single NPs), which would achieve 5 ms temporal resolution and 50 ms observation resolution.

Each SMNOBS shows a distinct LSPR spectrum (none of them is the same, Fig. 2E) and hence they can serve as multi-spectral (color) imaging probes for sub-diffraction imaging, as we demonstrated previously.[12] Such unique plasmonic optical properties effectively overcome the needs of multiple cycles of switching on and off fluorophores required by fluorescence nanoscopy, which potentially enables PHOTON to achieve much higher temporal resolutions.

Note that NPs (SMNOBS) scatter all visible wavelengths of light, as they are illuminated by a microscope illuminator (halogen lamp). Thus, the scattering intensity of single SMNOBS is the sum of scattering intensity at each wavelength of their LSPR spectra. Scattering intensity of single SMNOBS is orders of magnitude higher than fluorescence intensity of a single fluorophore (R6G), which permits single NPs to be detected and characterized by MSIS. The MSIS is equipped with an electric-cooled CCD camera (SonyICX 285) and LCTF (liquid-crystal tunable filter). This CCD camera is neither an EMCCD nor an ICCD. Thus, the recent report about potential modification of eqn (1) due to noise of EMCCD[41] is unrelated to this study. The LCTF allows rapid and simultaneous acquisition of LSPR spectra and images of multiple single NPs with 1 nm spectral resolution, enabling poly-dispersed NPs to serve as multicolor probes for super resolution imaging.[12]

Real-time probing of dynamic cascades of apoptotic signaling pathways of single live cells

We utilized PHOTON to image dynamic cascades of apoptotic signaling pathways of single live cells in real-time, which include binding of individual TNFα molecules with TNFR1 to form single L–R complexes and clusters of single complexes, their internalization (endocytosis), and subsequent cellular apoptosis. Representative snapshots of sequential super-resolution optical

 This journal is © The Royal Society of Chemistry 2012

Published on 04 January 2012 on http://pubs.rsc.org | doi:10.1039/C2NR11739H
Downloaded by Old Dominion University on 18 April 2012

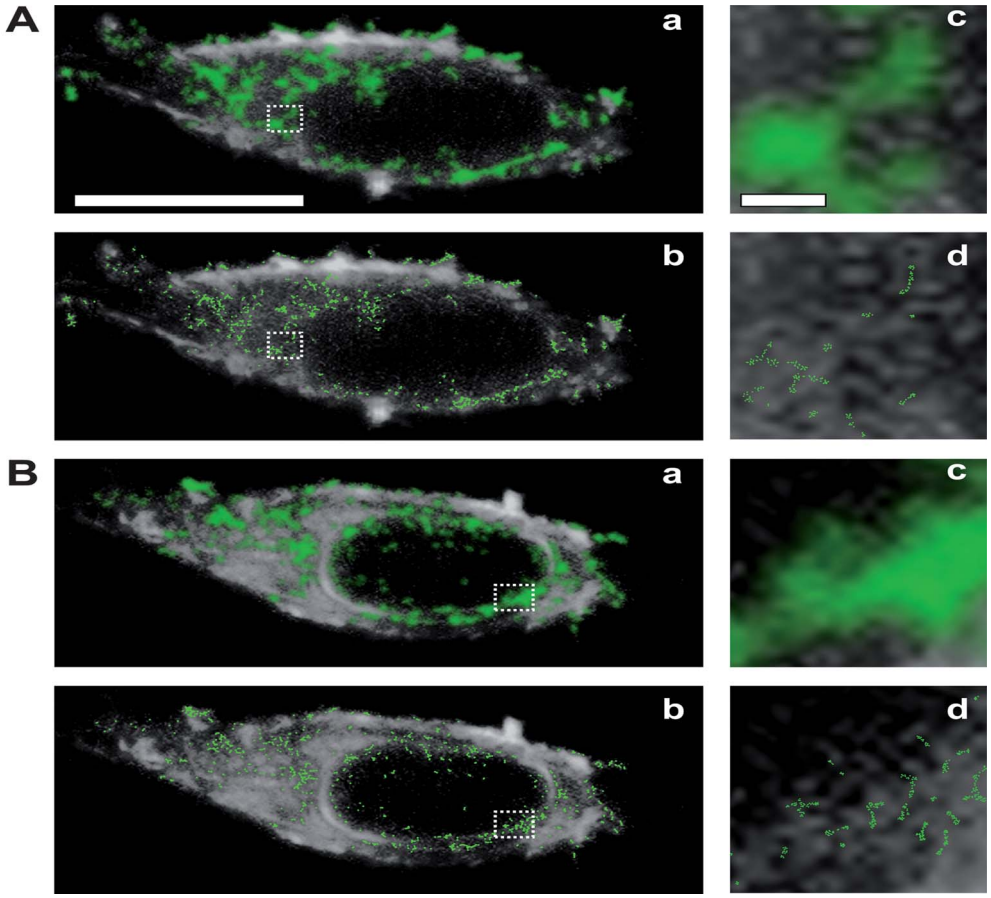


Fig. 5 Comparison of (a and c) optical diffraction-limited images and (b and d) super-resolution PHOTON images of single L–R complexes (bound SMNOBS): (A) on the surface and (B) inside single live cell (internalized SMNOBS), demonstrates superior super-resolution imaging capability of PHOTON. Zoom-in images of those squared in (a and b) are shown in (c and d). Scale bars are 10 μm in (a and b) and 0.5 μm in (c and d).

images of a single cell with the surface and internalized bound SMNOBS (complexes) are shown in Fig. 6 (Video S1†). More than 10 cells are imaged at single-cell level simultaneously, and 26 individual cells are studied for three repeated measurements of each experiment. To clearly illustrate individual L–R complexes (bound SMNOBS), a representative cell in each experiment (Fig. 6) and each control experiment (Fig. 7, S8 and S9†) is shown.

The sequential 2D images of the surface and cross-section of single live cells (5 μm in depth from the membrane surface) (Fig. 6) serve as effective and representative detection areas (volumes) to determine the number of bound SMNOBS on the surface of live cells, and inside the cells over time, respectively. This approach enables us to track the binding kinetics of single ligand with its receptor molecules, their diffusion and formation of their clusters on the surface of single cells, as well as the internalization of their clusters into the cells, and subsequent formation of larger internalized clusters inside the cells.

Plots of the number of surface L–R complexes of eight representative single cells (one line for each cell) *versus* their incubation time (Fig. 8A) show that the number of single L–R complexes on the surface of cells (surface complexes) and their binding kinetics vary widely among single cells. Plots of the number of internalized L–R complexes of single cells *versus* their incubation time (Fig. 8B) show that the number of single L–R complexes inside the cells (internalized complexes) and their internalization kinetics vary greatly among single cells. The cells with higher number of surface complexes have the higher number of internalized complexes.

The results show that the number of surface complexes of single cells increases with time and then decreases. In contrast, the number of internalized complexes starts to increase over time, 60–201 min after the formation of surface L–R complexes, and the delay varies widely among individual cells. The cells with higher number of surface complexes initiate internalization much sooner than those with the lower number. As internalization occurs, the number of surface complexes continues to increase and reaches a maximum prior to the decrease, indicating that binding of TNFα with TNFR1 continues and that their binding rates are higher than their internalization rates. As the internalization rates exceed the binding rates, the number of surface complexes decreases, while the number of intracellular complexes continues to increase.

Plots of the number of surface and internalized complexes of 26 single cells (one point for each cell) at their respective apoptosis time (as apoptosis starts) (Fig. 8C and D) show high dependence of apoptosis time of single cells upon the number of both their surface and internalized complexes. Wide ranges of

Published on 04 January 2012 on http://pubs.rsc.org | doi:10.1039/C2NR11739H
Downloaded by Old Dominion University on 18 April 2012

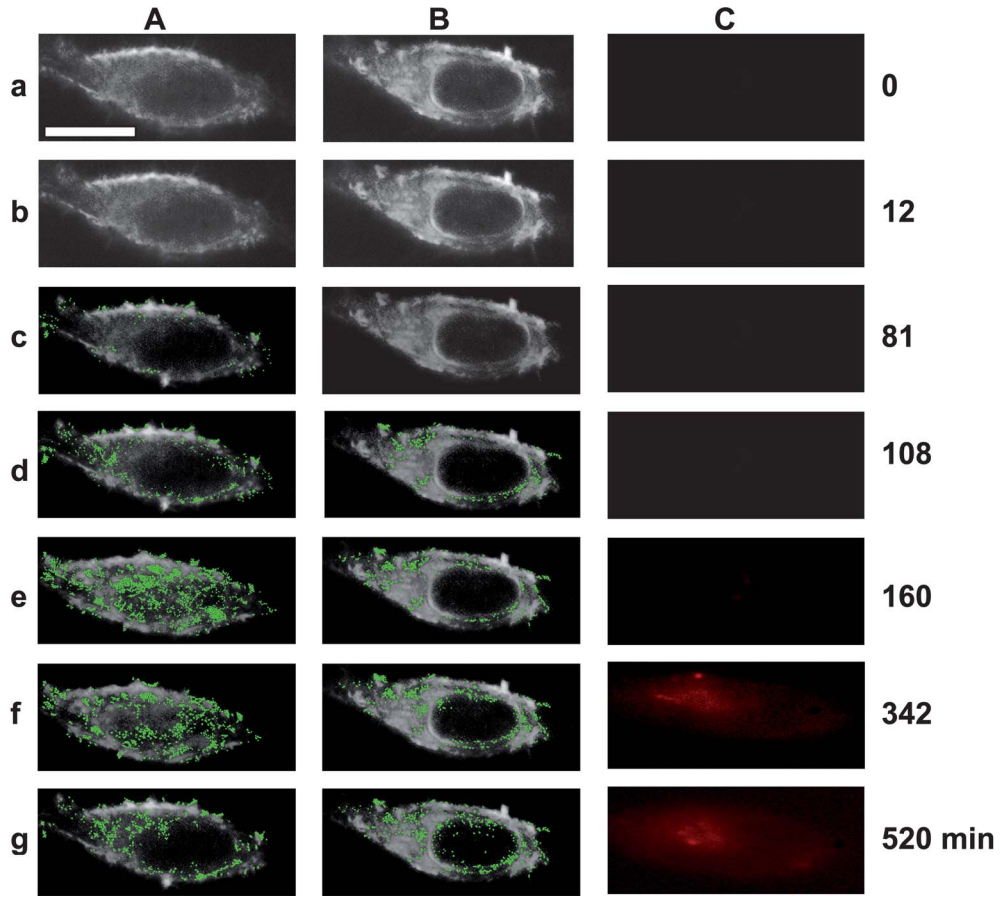


Fig. 6 Real-time tracking of dynamics and mechanisms of apoptotic pathways of single live cells incubated with SMNOBS (4.6 nM) over time using PHOTON. Snapshots of sequential dark-field super-resolution optical images of: (A) SMNOBS bound with TNFR1 to form single L–R complexes on the membrane of a live cell; (B) internalization of clusters of single L–R complexes into the cell (5 μm in-depth from the cell surface); and (C) fluorescence images of Magic Red (apoptosis assay) of the cytoplasm of the cell in (B), at (a) 0, (b) 12, (c) 81, (d) 108, (e) 160, (f) 342, and (g) 520 min. See real-time Video S1†. More than 10 cells (as one shown here) are imaged at single-cell level simultaneously for 900 min, and 26 individual cells are studied for three repeated measurements. The temporal and observation resolutions are 100 ms and 25 s, respectively. Scale bars are 10 μm for all images.

apoptosis time (t_a) are observed among single cells (Table S1†). Single cells with higher number of surface and internalized complexes exhibit earlier apoptosis than those with less number. By fitting the data points (measurements) of 26 cells using exponential equations (Fig. 8C and D), the minimal (critical) number of surface and internalized complexes for a cell to initiate apoptosis is determined as 21 and 33 complexes (TNFα molecules), respectively.

We also used PHOTON to track the diffusion of single L–R complexes, and to determine the formation of their clusters and the number of individual complexes (sizes) of each cluster in real-time at 1.3 nm resolution. We found that single surface complexes diffused to form small clusters on single cells, prior to their internalization into the cells. Plot of the number of surface complexes at the initial clustering time (as individual complexes start to form the clusters) shows that the timing of initiation of clustering of single L–R complexes highly depends upon the number of surface complexes. Initial clustering time varies dramatically among individual cells (Fig. 8E). Single cells with higher number of surface complexes form the clusters sooner than those with the lower number.

A plot of the number of surface clusters (each cluster with 2 or more complexes) of 26 cells at its respective internalization time (as initial internalization of clusters starts) (Fig. 8F) shows that individual cells have a wide range of initial internalization times. Single cells with higher number of surface clusters initiate their internalization sooner than those with lower number.

By fitting the data points (measurements) of 26 cells using exponential equations (Fig. 8E and F), the minimal number of surface complexes required for initiating the formation of the clusters is 19 (TNFα molecules) per cell, while only one cluster (2-complexes) per cell is needed for initiating its internalization. Interestingly, apoptosis of single cells occurs (t_a) at 222 to 519 min, varying widely among single cells, and only after endocytosis (t_e) of the clusters of single complexes (Table S1†).

Control experiments. The cells incubated with either medium alone or AgMMUA NPs (4.6 nM, absence of TNFα; blank control), or un-labeled TNFα (4.6 nM; positive control) were preformed simultaneously with the same number of cells (~10 cells per measurement and 26 cells in total for each control experiment) using the same approaches as described above.

 This journal is © The Royal Society of Chemistry 2012

Published on 04 January 2012 on http://pubs.rsc.org | doi:10.1039/C2NR11739H
Downloaded by Old Dominion University on 18 April 2012

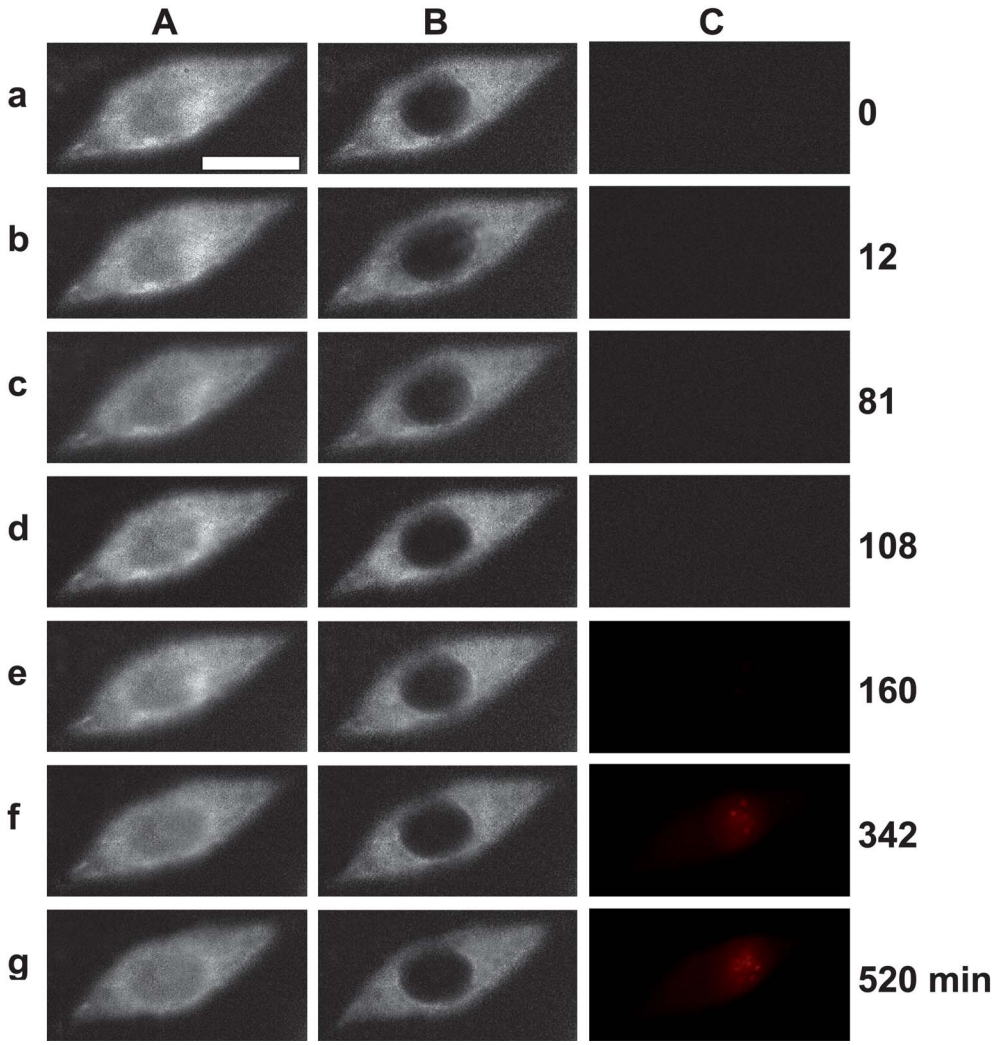


Fig. 7 Real-time tracking of dynamics and mechanisms of apoptotic pathways of single live cells incubated with TNFα (4.6 nM) (positive control experiment of Fig. 6). Snapshots of optical images of a single live cell: (A) on the membrane surface and (B) inside a live cell (5 μm in-depth from the cell surface); (C) fluorescence images of Magic Red (apoptosis assay) of the cytoplasm of the cell in (B), at (a) 0, (b) 12, (c) 81, (d) 108, (e) 160, (f) 342, and (g) 520 min. About 10 individual cells are imaged simultaneously for 900 min, and more than 26 individual cells are studied for three measurements. The percentages of cells that became apoptotic were 3.8% at 282 min, 15.4% at 342 min, 15.4% at 360 min, 23.1% at 381 min, 11.5% at 402 min, 7.7% at 462 min, 7.7% at 520 min, 3.8% at 582 min, 3.8% at 621 min, 4.0% at 642 min and 3.8% at 720 min. The temporal resolution is 100 ms and observation resolution is 25 s. Scale bar is 10 μm for all images.

Sequential dark-field optical images (Fig. S8AB†) and fluorescence images (Fig. S8C†) of one representative cell of 26 cells incubated with the medium show the absence of red fluorescence of apoptosis assay (Magic Red), demonstrating that the cell remains non-apoptotic for 900 min over the course of entire experiment. Thus, the apoptotic cells observed in Fig. 6 are not attributed to the long period of imaging time, but binding with SMNOBS.

Sequential dark-field optical images (Fig. S9AB†) and fluorescence images (Fig. S9C†) of one representative cell of 26 cells incubated with AgMMUA NPs show the absence of plasmonic green colors of SMNOBS, and red fluorescence of Magic Red, demonstrating that AgMMUA NPs do not attach onto the cell surface (non-specific interactions), do not internalize into the cells and do not cause cellular apoptosis. Note that only bound and internalized SMNOBS stay on the focal plane of PHOTON, which enables them to be imaged. Thus, what we observed (Fig. 6, Table S1†) is attributed to specific binding of TNFα (AgMMUA–TNFα) with TNFR1 on single live cells, which led to cellular apoptosis.

Sequential dark-field optical images (Fig. 7A and B) and fluorescence images (Fig. 7C) of one representative cell of 26 cells incubated with TNFα (unlabeled with NPs) show that cellular apoptosis occurs at the same time frame (t_a) as the cells incubated with the same concentration of SMNOBS (4.6 nM), ranging from 282 to 720 min (Table S1†). The results indicate that SMNOBS act the same way as unlabeled TNFα to initiate cellular apoptosis; and conjugated NPs (Fig. 2A) have little effects on the study of apoptotic signaling pathways, and NPs are successfully used to probe single ligand induced signaling pathways of single cells in real-time.

Published on 04 January 2012 on http://pubs.rsc.org | doi:10.1039/C2NR11739H
Downloaded by Old Dominion University on 18 April 2012

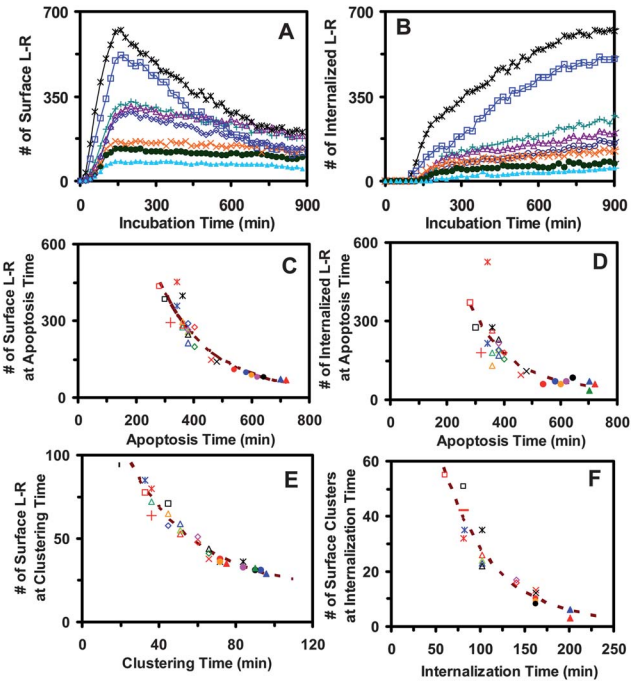


Fig. 8 Study of dependence of dynamics and mechanisms of apoptotic pathways of single live cells on the number of single L–R complexes on/in single cells. Plots of the number of (A) surface and (B) internalized single L–R complexes *versus* incubation time of cells with SMNOBS show that they vary widely among individual cells (each curve represents a live cell). Plots of the number of (C) surface and (D) internalized L–R complexes of single cells at their initial apoptosis time (as apoptosis starts) show that the cells with higher number of surface and internalized complexes become apoptotic sooner than those with lower number. (E) Plot of the number of single surface complexes as they start to form the clusters (clustering time) on the cells shows that the cells with higher number of surface complexes start to form clusters sooner. (F) Plot of the number of representative surface clusters (each with 3-complexes) at initial internalized time (as clusters start to internalize) shows that the cells with higher number of surface clusters start to internalize sooner. Each point in (C–F) represents a live cell. Points are experimental data and dashed lines are theoretic fitting *via* exponential equations: (C) $N_b = 21 + 2.1 \times 10^3 e^{-0.0059 t_a}$ and (D) $N_i = 33 + 2.3 \times 10^3 e^{-0.0068 t_a}$, where N_b and N_i are the number of surface L–R binding complexes and internalized complexes at the initial apoptosis time (t_a), with regression (R^2) of 0.89 and 0.64, respectively; (E) $N_b = 19 + 156 e^{-0.028 t_c}$ and (F) $N_c = 1.1 + 157 e^{-0.018 t_i}$, where N_b and N_c are the number of surface L–R binding complexes and clusters at the initial clustering time (t_c) and internalized time (t_i), with regression (R^2) of 0.97 and 0.92, respectively.

Real-time study of apoptotic dynamics and mechanisms of single live cells

To study the dependence of cellular apoptosis on sizes, number and formation dynamics of clusters, we plot the distribution of sizes and number of surface and internalized clusters at initial apoptosis times for 26 individual cells (Fig. 9A, 10A). The results show that the sizes and number of clusters and initial apoptosis times vary widely among individual cells. Single SMNOBS binds with TNFR1 on the surface of single cells to form single L–R complexes (t_b), following the formation of their clusters, then internalization of the clusters (t_e), which finally lead to apoptosis (t_a) of the cells (Table S1†). The formation of surface clusters occurs prior to their internalization into the cells, and none of single L–R complexes is observed inside the cells, which indicate that formation of clusters on the surface of cells is essential to their internalization. Furthermore, apoptosis occurs (t_a) only and long after internalization of clusters occurs (t_e), and only cells with internalized clusters become apoptotic, which shows that the formation of surface clusters and their internalization are essential to cellular apoptosis.

To clearly present formation of various sizes and number of clusters on/in individual cells over time, we select four representative cells from 26 individual cells (cells 1, 4, 16, and 26 in Table S1†) as examples, and plot the number of various sizes of the surface and internalized clusters *versus* incubation time (Fig. 9B and 10B).

Cell-1 (Fig. 9a and 10a) has the largest surface and internalized clusters (each with 5–6 complexes) and its apoptosis starts the soonest at 282 min. In contrast, cell-4 (Fig. 9b and 10b) has the same number of smaller surface and internalized clusters (2–4 complexes) as cell-1, but not large clusters; its apoptosis starts much later at 342 min. Cell-16 (Fig. 9c and 10c) and cell-26 (Fig. 9d and 10d) have the smallest clusters (2–3 complexes) only, and both show much slower apoptosis at 406 and 720 min than those cells with large clusters (cell-1 and cell-4), respectively.

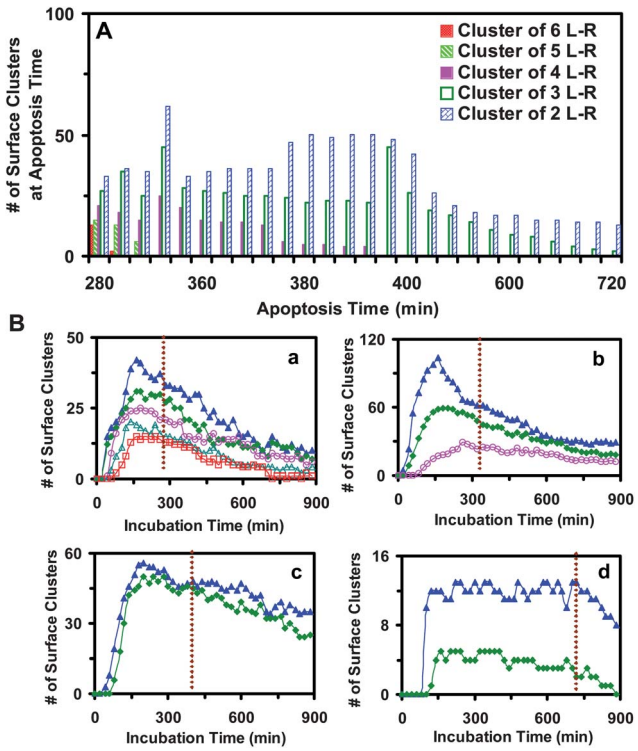


Fig. 9 Real-time study of dependence of apoptotic dynamics of single live cells upon the number and sizes of their *surface* clusters. (A) Number of surface clusters (each with 2–6 complexes) at initial apoptosis times of single live cells varies widely among single cells. Each group of bars represents one of 26 cells in Table S1†. (B) Plots of the number of surface clusters *versus* incubation time for four representative individual cells: (a) cell-1; (b) cell-4; (c) cell-16; and (d) cell-26 show that their initial apoptosis occurs at 282, 342, 402 and 720 min, as indicated by a vertical dashed line, respectively. Six symbols represent various sizes of the clusters, each with (▲) 2; (♦) 3; (○) 4; (△) 5; and (□) 6 L–R complexes.

This journal is © The Royal Society of Chemistry 2012

Published on 04 January 2012 on http://pubs.rsc.org | doi:10.1039/C2NR11739H
Downloaded by Old Dominion University on 18 April 2012

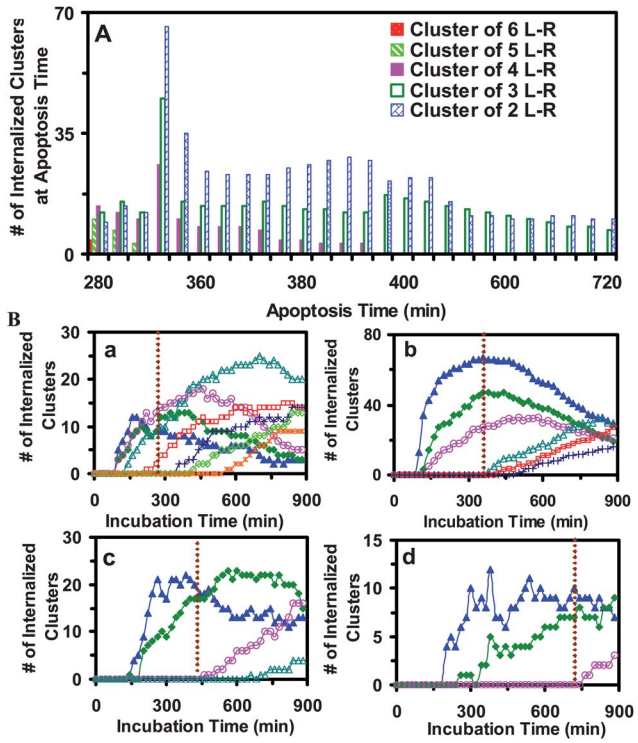


Fig. 10 Real-time study of dependence of apoptotic dynamics of single live cells upon the number and sizes of their *internalized* clusters. (A) Number of internalized clusters (each with 2–6 complexes) at initial apoptosis times of single live cells varies broadly among individual cells. Each group of bars represents one of 26 cells in Table S1†; (B) plots of the number of clusters *versus* incubation time for four representative cells: (a) cell-1; (b) cell-4; (c) cell-16; and (d) cell-26 show that their initial apoptosis occurs at 282, 342, 402 and 720 min, as indicated by a vertical dashed line, respectively. Eight symbols represent various sizes of the clusters with each cluster of (▲) 2, (◆) 3, (○) 4, (△) 5, (□) 6, (+) 7, (◇) 8, and (✱) 9 L–R complexes.

Cell-16 has about 20 times more surface clusters and twice more internalized clusters (3-complexes) than cell-26, and it shows much sooner apoptosis than cell-26. The results show the high dependence of cellular apoptosis dynamics upon the sizes and number of surface and internalized clusters. The cells with larger sizes and higher number of larger surface and internalized clusters become apoptotic faster than those cells with smaller sizes and less number of clusters.

We also observed the high dependence of internalization dynamics of clusters upon the sizes and formation dynamics of the surface clusters (Fig. 9B and 10B). For example, cell-1 forms its surface clusters (each with 2–6 complexes) at 60 min of its incubation with SMNOBS. Internalized clusters (each with 2–4 complexes) are observed at 102 min. Interestingly, the larger internalized clusters (6-complexes) are found at 222 min, which is 120 min later than the observation of the smaller internalized clusters (2–4 complexes) (Fig. 9a and 10a). The results suggest that smaller clusters internalize faster and more favorably than larger clusters. The higher number of smaller surface clusters may also attribute to their faster endocytosis. As apoptosis starts at 292 min, the surface clusters (2–6 complexes) continue to internalize. Only long after apoptosis occurs, the internalized clusters form the larger clusters (each with 7–9 complexes) inside the cells at 360, 420 and 561 min, respectively. Their numbers increase with time as apoptosis progresses.

Similar phenomena are observed for other cells. For instance, cell-4 forms its surface clusters (each with 2–4 complexes) at 42 min, which start to internalize into the cell at 102, 120 and 141 min, respectively. As the cell initiates apoptosis at 342 min, the surface clusters (2–4 complexes) continue their internalization. After the cell initiates apoptosis, the internalized clusters form larger clusters (5–7 complexes) inside the cells, at 381, 420 and 501 min, respectively. Cell-16 forms its surface clusters (each with 2–3 complexes) at 42 and 81 min, respectively, which start to internalize at 142 min. As the cell initiates apoptosis at 402 min, the surface clusters continue to internalize. After apoptosis occurs, the internalized clusters start to form the larger intracellular clusters (each with 4–5 complexes) at 462 and 660 min, respectively. Cell-26 forms its surface clusters (each with 2 or 3 complexes) at 102 and 120 min, which start to internalize at 201 and 261 min, respectively. As apoptosis occurs at 720 min, the surface clusters continue to internalize. The internalized clusters then form larger intracellular clusters (each with 4 complexes) at 762 min, which is long after apoptosis starts. Similar phenomena are observed for all other individual cells (Table S1†).

We also determined how single L–R complexes form the clusters on the surface of cells, and how internalized clusters form the larger cluster inside the cells, by tracking their diffusion at nm resolution over time using the same approaches as described above. The results show that majority of surface and internalized clusters (61% and 68%) increase their sizes gradually and in an orderly manner, from individual complexes (or the smallest internalized clusters, each with 2-complexes) to small, from the small to the medium size, and from the medium to larger clusters. Notably, a few surface and internalized clusters (39% and 31%) are formed directly from individual complexes or the smallest internalized clusters (each with 2-complexes), respectively. The results suggest that random diffusion of single complexes and their smaller clusters is most likely attributed to their clustering.

Taken together, the results show that: (i) internalization dynamics of the clusters highly depends upon the formation dynamics of given sizes and number of surface cluster and (ii) apoptotic dynamics highly rely upon the internalization dynamics of the surface clusters, and their sizes and number. The larger clusters play more significant roles in initiating earlier apoptosis than the high number of smaller clusters. The results suggest the possibility of controlling cellular apoptosis by tuning and inhibiting the binding of ligand with its receptors, the formation of clusters of single L–R complexes on single cells, and their internalization into the cells.

Notably, the results (Fig. 6–10) show that the formation of clusters depends upon the number of single L–R complexes (binding of SMNOBS with TNFR1) on single cells, which leads to internalization of clusters, and subsequent apoptosis of the cells. Thus, the binding triggers biological functions and shows underlying biological implications. The binding leads to formation of small, medium, and then large clusters, showing that the clustering occurs in an orderly and controllable manner. These phenomena are very unlike aggregation of NPs that would occur in an uncontrollable fashion, and lead to massive aggregation of NPs and change of plasmonic colors (significant red-shift of

Published on 04 January 2012 on http://pubs.rsc.org | doi:10.1039/C2NR11739H
Downloaded by Old Dominion University on 18 April 2012

LSPR spectra) of NPs. In addition, SMNOBS does not lead to the aggregation of NPs, as shown in the study of binding of much higher concentrations of SMNOBS (50 nM) with MAB (0–500 nM) in the buffer solution (Fig. S3†).

Furthermore, the blank control experiments (Fig. S9†) show that the presence of AgMMUA NPs does not lead to aggregation of NPs. Moreover, TNFα molecules non-conjugated with NPs (positive control experiment in Fig. 7) initiate cellular apoptotic kinetics as the labeled ones (SMNOBS), showing that conjugated NPs do not affect the initiation of apoptosis. Therefore, this study shows that the formation of clusters is not attributed to the labeled NPs, but TNFα itself, and NPs can serve as effective and biocompatible probes for the study of signaling pathways of single live cells in real-time at SM and nm resolutions.

Real-time tracking of diffusion mechanisms of single L–R complexes and their clusters

We observed that single L–R complexes diffused on the surface (plasma membrane) of single live cells to form surface clusters, which then internalized into the cells to initiate cellular apoptosis. To determine whether their diffusion mechanisms follow random Brownian diffusion, directed diffusion or restrict diffusion,[42–44] we tracked the diffusion trajectories of individual complexes and their surface and internalized clusters in real-time at nm resolution using PHOTON (Video S2†). We studied the diffusion of clusters with various sizes of single L–R complexes, and presented the diffusion of representative clusters (each with 3 L–R complexes), as an example, to show the diffusion mechanisms of clusters and capabilities of PHOTON.

To overcome the heterogeneity of cellular environments, we used real-time square-displacement (RTSD, square of diffusion distance at a given time interval),[13,16,45] instead of mean (average) square-displacement (MSD), to determine their diffusion mechanisms over time. Plots of RTSD *versus* diffusion time show the linearity (Fig. 11), indicating that the diffusion modes of (A) individual L–R complexes and (B) their surface clusters on single live cells, and (C) the internalized clusters inside the cells follow simple Brownian diffusion, but not directed diffusion.

Using random-walk theory (RTSD = 4DΔt, where D is the diffusion coefficient and Δt is the diffusion time) and slopes of the linear portions of the plots in Fig. 11, the diffusion coefficients of single complexes, and its clusters (3-complexes) on/in single cells are determined as $(2.8 \pm 0.2) \times 10^{-11}$, $(9.6 \pm 2.8) \times 10^{-12}$ and $(1.3 \pm 0.2) \times 10^{-10}$ cm^2 s^{-1}, respectively. The results agree excellently with those reported about L–R complexes on the same type of cells (L929).[43,44]

The Stoke–Einstein equation, $D = kT/(6\pi\eta a)$, states that the diffusion coefficient (D) depends on the radii (a) of solute (individual complexes or their clusters) and viscosity of medium (η). The size of single clusters (3-complexes) is about three times larger than single complexes. Thus, their diffusion coefficient is about one-third of single complexes, since both are situated on the membrane of single live cells with the same viscosities. Notably, the surface and internalized clusters have the same size (3-complexes). The results show that diffusion coefficients of single internalized clusters are ~14 times larger than the surface clusters, indicating that viscosity of the plasma membrane of single live cells is ~14 times higher than their cytoplasm, which agrees well with those reported previously.[46,47]

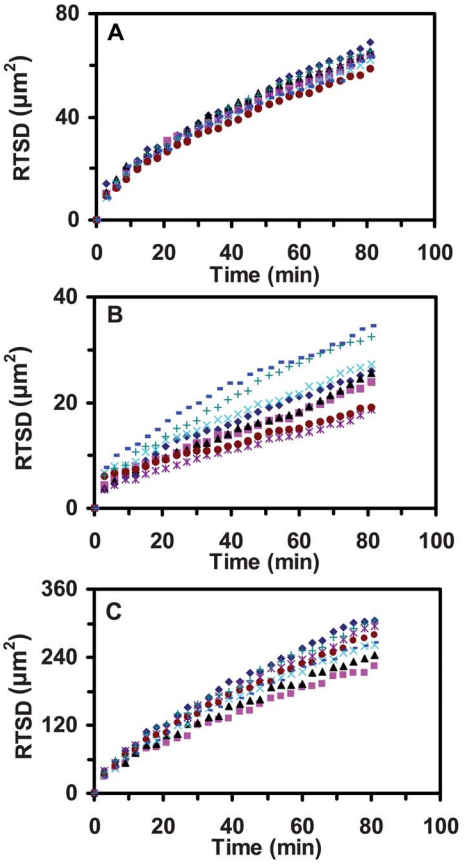


Fig. 11 Characterization of diffusion mechanisms and diffusion coefficients of (A) single L–R complexes and (B) its clusters (each with 3-complexes) on single live cells; and (C) the clusters (each with 3-complexes) inside the cells. Plots of real-time square displacement (RTSD) as a function of time show high linearity over time, indicating random Brownian diffusion with diffusion coefficients of (A–C) as $(2.8 \pm 0.2) \times 10^{-11}$, $(9.6 \pm 2.9) \times 10^{-12}$ and $(1.3 \pm 0.2) \times 10^{-10}$ cm^2 s^{-1}, respectively. Each symbol represents a cell with individual (A) surface L–R complexes, (B) surface cluster, and (C) internalized cluster of the complexes. Data from 8 representative cells (Fig. 8, Table S1†) are shown as 8 different symbols in (A–C): (▬) cell-1; (✚) cell-3; (✖) cell-6; (◆) cell-8; (✖) cell-16; (▲) cell-18; ●, cell 22; and (■) cell-26.

Diffusion distances of single complexes, their clusters (3-complexes) on/in single cells within the observation resolution (25 s) of PHOTON are calculated using their diffusion coefficients and random-walk theory. The results show that their diffusion distances within 25 s are (0.037 ± 0.010), (0.022 ± 0.012), and (0.081 ± 0.032) μm, respectively. The spatial resolutions of PHOTON are (1.5 ± 0.2) nm. The DFOMS, equipped with an objective with numerical apertures of 1.2–1.43 (oil), offers the depth of the field (DOF, focal plane) of ~0.19 μm. Therefore, PHOTON can determine the diffusion distances within its observation resolution of 25 s, as well as its DOF (z-direction). Taken together, the results (Fig. 11) show that PHOTON can track diffusion mechanisms of single L–R complexes and their clusters on/in single cells in real-time at nm resolution, and they follow random Brownian diffusion mode.

This journal is © The Royal Society of Chemistry 2012

Published on 04 January 2012 on http://pubs.rsc.org | doi:10.1039/C2NR11739H
Downloaded by Old Dominion University on 18 April 2012

Summary

In summary, we have successfully developed and used PHOTON to map the dynamic cascades and molecular mechanisms of apoptotic signaling pathways of single live cells in real-time at SM and nm resolutions. As summarized in Fig. 12, the results show that the binding of single ligand (TNFα) molecules with their receptor (TNFR1) on single live cells initiates at 9 to 42 min of their incubation with SMNOBS, which varies significantly with the number of TNFR1 molecules on each cell. Individual surface complexes on single cells diffuse randomly to form various sizes of surface clusters (2–6 complexes) at 33 to 96 min, while endocytosis of the surface clusters into the cells starts at 60 to 201 min. Both vary broadly upon the number of surface complexes on each cell. The minimal (critical) number of surface complexes needed to initiate formation of surface clusters on a cell is 19 molecules, while only one cluster (2-complexes) is needed to initiate its endocytosis into a cell. Formation of surface clusters is essential to their endocytosis, which is required for cellular apoptosis. The apoptosis of single cells starts between 282 and 720 min, which varies widely upon the size and number of surface and internalized clusters of each cell. The larger size and higher number of surface and internalized clusters of single cells lead to their earlier apoptosis. Notably, the sizes of the clusters play more significant roles in initiating cellular apoptosis than their numbers. The results suggest the possibility of tuning and inhibiting signaling pathways by controlling formation of single L–R complexes and their clusters. This study provides new insights into sophisticated dynamic cascades and molecular mechanisms of signaling pathways of single live cells, which is crucial to better understand cellular functions and design more effective therapies. This study also demonstrates powerful capabilities of PHOTON and superior biocompatibility and photostability of SMNOBS for real-time super-resolution SM imaging of single live cells, especially for probing of challenging cellular signaling transduction pathways.

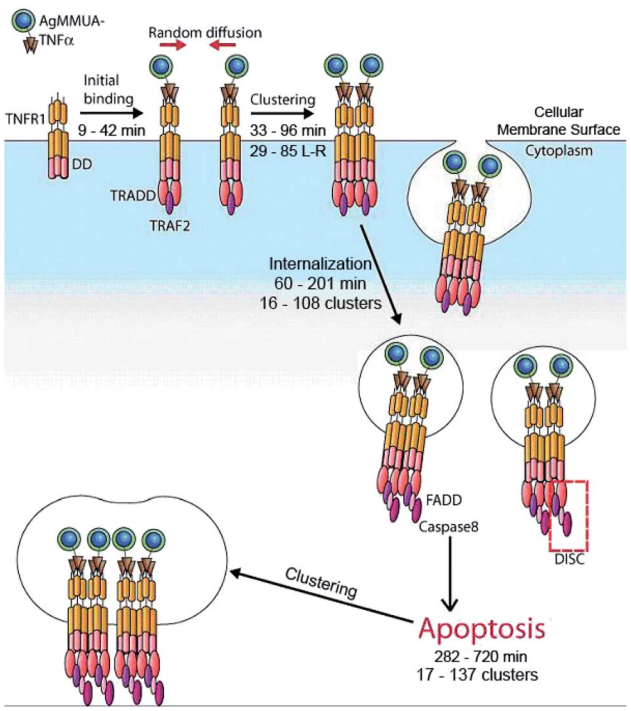


Fig. 12 Schematic illustration summarizes dynamics and molecular mechanisms of apoptotic signaling pathways of single cells, triggered by the binding of single TNFα molecules with TNFR1, determined by PHOTON.

Experimental section

Reagents and supplies

Silver nitrate (99.9%), sodium borohydrate (98%), sodium citrate dihydrate (99%), hydrogen peroxide (30%), polyvinylpyrrolidone (PVP), 6-mercapto-1-hexanol (MCH) (97%), and 11-mercaptoundecanoic acid (MUA) (95%) were purchased from Sigma-Aldrich, and used as received. Human recombinant tumor necrosis factor α (TNFα) and its monoclonal antibody (MAB) (R&D), *n*-hydroxysulfosuccinimide (sulfo-NHS, 98.5%, Pierce), 1-ethyl-3-(3-dimethylaminopropyl)-carbodiimide hydrochloride (EDC, 99%, Pierce), Magic Red (Immunochemistry Technologies), Dulbecco's modified Eagle's medium (DMEM, ATCC), 100× penicillin–streptomycin–glutamine solution (P-S-G, ATCC), fetal bovine serum (FBS, ATCC), Hanks' balanced salt solution (HBSS, without Ca^{2+}, Mg^{2+} and phenol red, pH 7.4, ATCC), and mouse fibroblast cells (L929, ATCC) were also purchased. All solutions, including phosphate buffer saline (PBS, 10 mM, pH 7.4), were prepared using deionized (DI) water (18 MΩ, Barnstead).

Synthesis and characterization of SMNOBS (AgMMUA–TNFα NPs)

2.6 nm Ag NPs. Ag NPs with average diameters of 2.6 ± 1.1 nm were synthesized and characterized, and then functionalized with a mixed monolayer of MUA and MCH, as we described previously.[11,12,48] Briefly, freshly prepared solutions of $AgNO_3$ (0.11 mM), sodium citrate (1.91 mM), PVP (0.052 mM), and H_2O_2 (25.0 mM) in DI water (42.3 mL) were well mixed under stirring. $NaBH_4$ (150 μL, 100 mM) was then added into the mixture under stirring for 3 h to synthesize Ag NPs.

The solution was filtered using 0.2 μm membrane filters, washed thoroughly with DI water *via* centrifugation, and immediately characterized using high-resolution transmission electron microscopy (HRTEM) (JEOL JEM-2100F), UV-vis spectroscopy (Hitachi U3310), dynamic light scattering (DLS) (Nicomp 380ZLS particle sizing system), and our dark-field optical microscopy and spectroscopy (DFOMS, also named as **s**ingle **n**anoparticle **o**ptical **m**icroscopy and **s**pectroscopy, SNOMS, by us).

AgMMUA NPs. AgMMUA NPs were prepared by mixing freshly prepared Ag NPs (50 mL, 154 nM) with MUA (10 mM) and MCH (90 mM) to have final concentrations of MUA, MCH and Ag NPs at 0.1 mM, 0.9 mM, and 152 nM, respectively.[11] The mixture was stirred for 24 h to attach MUA and MCH onto the surface of NPs *via* the interaction of –SH groups with NPs, and SN2 replacement reaction of citrate molecules with MUA and MCH (Fig. 2A).[11] The AgMMUA NPs were washed thrice using DI water to remove excess MUA and MCH using centrifugation, and immediately characterized using UV-vis spectroscopy, DLS

Published on 04 January 2012 on http://pubs.rsc.org | doi:10.1039/C2NR11739H
Downloaded by Old Dominion University on 18 April 2012

and DFOMS. NMR samples were immediately prepared by drying the washed AgMMUA NPs using a lyophilizer (VirTis) and dissolving AgMMUA NPs (50 mg) in D_2O (1 mL), and characterized by NMR (400 MHz, Bruker).

AgMMUA–TNFα NPs (SMNOBS). AgMMUA NP aqueous solution (50 mL, 154 nM) was mixed with EDC (77 μmol) and sulfo-NHS (7.7 μmol) under stirring at room temperature for 40 min, to form AgMMUA-NP-s-NHS esters. The AgMMUA-NP-s-NHS was isolated using a Centriprep YM-30 (Millipore) *via* centrifugation.

TNFα was then added to AgMMUA-NP-s-NHS in the buffer with a molar ratio of TNFα to AgMMUA NPs at 0.97. The solution was mixed using a rotary shaker at room temperature for 2 h and then at 4 °C for 12 h to synthesize AgMMUA–TNFα NPs. The AgMMUA–TNFα NPs were thoroughly washed with PBS buffer to remove excess TNFα using centrifugation at 4 °C, and resuspended in the buffer, which was characterized using UV-vis spectroscopy, DLS and DFOMS. Concentrations of Ag, AgMMUA, and AgMMUA–TNFα NPs are calculated using similar approaches as we described previously.[16,45,49]

Characterization of affinity and photostability of SMNOBS

We measured the binding constant (affinity) of SMNOBS with MAB in the PBS buffer by measuring the absorbance of SMNOBS (50 nM) incubated with their MAB (0, 10, 100, 200 and 500 nM) over time using similar approaches as we described previously.[11,14] We acquired the UV-vis absorption spectra of the mixture at room temperature every 5 min for the first 2 h, then at every 2.5 h until 48 h. We stored the mixture at 4 °C between each spectroscopy measurement to avoid denaturation of proteins.

We characterized photostability of single SMNOBS using the approach as we described previously.[11,13] We acquired sequential optical images and scattering intensity of single SMNOBS using DFOMS with the exposure time of 100 ms and readout time of 40.6 ms, while these NPs were constantly irradiated under a dark-field microscope illuminator (100 W halogen) for 12 h[11,13] The illumination power at the sample stage (focal plane of the dark-field) was 0.070 ± 0.001 W, as measured by a power meter (Melles Griot). The minimal 300 individual SMNOBS were characterized for three repeated measurements with 100 single SMNOBS per measurement.

Real-time super-resolution single-molecular imaging of single live cells

The cells (L929) cultured on sterilized microscope coverslips were incubated with SMNOBS (4.6 nM) in homemade micro-chambers. Individual SMNOBS bound with TNFR1 (L–R complexes), their diffusions to form clusters on the membrane of single live cells and internalization of clusters into the cells (5 μm in-depth from cellular membrane) were imaged over 900 min in real-time using DFOMS.

We have fully described our DFOMS for real-time imaging and spectroscopic characterization of single NPs in solutions,[10,11,48] single live cells[14,17–19,50] and embryos.[13,16] In this study, the microscope is equipped with a dark-field condenser (oil, 1.43–1.20), a microscope illuminator (halogen lamp, 100 W), a 100× objective (Plan fluor 100×, N.A. 0.5–1.3), and a Multi-spectral Imaging System (MSIS), N-MSI-VIS-FLEX, Cambridge Research Inc. (CRi, Hopkiton, MA), which is an integrated system of a CCD camera (SonyICX 285) and LCTF.[51] The CCD camera is an electric-cooled (0 °C) CCD camera, but not an EMCCD or ICCD camera.

As determined experimentally and theoretically, one electron count (analog-to-digital count, ADC) of our CCD camera with a 12 bit scale is equal to the collection of ~3.5 electrons (photons) with a gain setting of 1.0. Scattering intensity of individual SMNOBS (or cluster) in ADC was determined by subtracting integrated intensity of a pixel area where SMNOBS are absent (blank) from the same size of pixel area where single SMNOBS (cluster) are present using similar approaches as we described previously.[10–12,14,16] The scattering intensity of single SMNOBS in ADC was then converted to photons using the ratio of ADC to electron (photons) at 3.5.

The microscope is also equipped with an automatically controlled motorized microscopic stage, which enables auto-focusing and precisely controlling of *z*-locations for mapping in the *z*-direction. Three reference points on each slide were chosen to correct any possible stage drift during each experiment.

Fluorescence images of Magic Red (apoptotic assay) inside the cells were also acquired in real-time using an epi-fluorescence microscope, which is equipped with a filter cube (Chroma Tech) containing a band-pass (bp) excitation filter (546 ± 10 nm), a bp emission filter (605 ± 30 nm) and a dichroic mirror (565 nm).

Stacks of optical images of the clusters of single L–R complex on/in single live cells were acquired from 450 to 700 nm with 100 ms exposure time at each nm using DFOMS equipped with MSIS. The LSPR spectra of single clusters were deconvoluted using the LSPR spectrum of single SMNOBS *via* the Cauchy–Lorentz model,[38,39] to determine the number of single SMNOBS bound with TNFR1 located within the optical diffraction limit. Their centroids (precise locations) were determined using PSF. The measurement was repeated 20 times for each bound SMNOBS, generating its centroid distribution.

The number of single complexes with precise locations at sub-nm spatial resolution was determined by fitting the distribution using 2D Gaussian. LSPR spectra of each bound SMNOBS at given precise positions determined by PHOTON were acquired to validate that their sum matched with the convoluted LSPR spectra of individual clusters. Using such approaches, the total number of single surface and internalized L–R complexes of single cells in each representative detection area (volume) was imaged at 1.5 ± 0.2 nm spatial and 100 ms temporal resolutions over time for 900 min (Table S1†). The snapshots of sequential images over 540 min are presented in Fig. 6, 7, S8 and S9 (Table S1†).

Two blank control experiments (in the absence of SMNOBS) and one positive control experiment (in the presence of unlabeled TNFα) were performed simultaneously in real-time using the same approaches for each experiment as described above: (i) cells incubated with the cell culture medium alone; (ii) cells incubated with 4.6 nM AgMMUA NPs (non-conjugated with TNFα); and (iii) cells incubated with 4.6 nM TNFα (non-conjugated with NPs).

 This journal is © The Royal Society of Chemistry 2012

Published on 04 January 2012 on http://pubs.rsc.org | doi:10.1039/C2NR11739H
Downloaded by Old Dominion University on 18 April 2012

Design and data analysis of PHOTON for super-resolution imaging of single live cells

Stacks of plasmonic images (image cubes) of single AgMMUA–TNFα–TNFR1 NPs (SMNOBS bound with TNFR1, L–R complexes) on and in single live cells were acquired from 450 to 700 nm at each nm (1 nm spectral resolution) with 100 ms exposure time using MSIS, as shown in Fig. 4A. The LSPR spectra of clusters of the bound SMNOBS located within the optical diffraction limit were deconvoluted using the LSPR spectrum of individual SMNOBS *via* the Cauchy–Lorentz distribution model (Fig. S4A and S6A†), as described in eqn (2):[38,39,52,53]

$$I(\lambda) = \sum_{i=1}^{n} \frac{a_i}{\left[1 + \left(\frac{\lambda - \lambda_i}{b_i}\right)^2\right]} \quad (2)$$

where n is the total number of individual NPs (bound SMNOBS); $I(\lambda)$ is the scattering intensity of cluster of individual NPs at a given wavelength (λ); a_i is the peak intensity; λ_i is the peak wavelength (λ_{max}); and b_i is the half of FWHM of the LSPR spectrum of the i^{th} NPs.

Using Matlab curve fitting tools with the customized eqn (2), each spectrum of the cluster in either Fig. S4A or S6A† was fitted. The range of a_i from 0 to infinity, the range of λ_i from 510 to 620 nm, and of b_i from 25 to 45 nm (determined by the λ_{max} and FWHM of LSPR spectra of single SMNOBS in Fig. 2E) were used for fitting the spectrum in either Fig. S4A or S6A†. The total number of single SMNOBS in each cluster was determined by the best fitting curve of the spectrum with the highest regression (R^2).

The number of SMNOBS located within the optical diffraction limit (each spot) is also determined by their scattering intensity, since their scattering intensity is proportional to the number of SMNOBS in the spot.

The LSPR spectrum of each NP (SMNOBS) is described by eqn (3):

$$I_i(\lambda) = \frac{a_i}{\left[1 + \left(\frac{\lambda - \lambda_i}{b_i}\right)^2\right]} \quad (3)$$

where $I_i(\lambda)$ is the scattering intensity of the i^{th} NP at a given wavelength (λ). Notably, a_i, λ_i and b_i are determined by the spectral curve fitting using eqn (2).

Using the deconvoluted LSPR spectra of individual SMNOBS (Fig. S4A(a–d)†) obtained from eqn (3), the image cubes of the clusters, as those circled in Fig. 4A, are unmixed (deconvoluted) at the given wavelength of each SMNOBS. For n number of SMNOBS, n images are generated in TIFF format. Each image is the profile of scattering intensity of a SMNOBS with its deconvoluted LSPR spectrum *versus* its location in the full-frame CCD array (Fig. S4B and S6B†).

The deconvolution (un-mixing) of each image cube was performed using the software of MSIS, as described in eqn (4) and (5). Note that each image cube of the cluster at each pixel is made up of a linear combination of LSPR spectra of individual NPs at the pixel:[54]

$$\boldsymbol{S}_{x,y} = L\boldsymbol{w} \quad (4)$$

$$\boldsymbol{S}_{x,y} = \begin{bmatrix} L_{11} & L_{12} & \ldots & L_{1n} \\ L_{21} & L_{22} & \ldots & L_{2n} \\ \ldots & \ldots & & \ldots \\ L_{m1} & L_{m2} & \ldots & L_{mn} \end{bmatrix} \begin{bmatrix} w_1 \\ w_2 \\ \ldots \\ w_n \end{bmatrix} \quad (5)$$

where $\boldsymbol{S}_{x,y}$ is a vector containing multiple LSPR spectra of the cluster at a pixel; L is a matrix with n LSPR spectra from n number of individual NPs; m is the number of spectral channels; and $\boldsymbol{w}$ is a vector of scattering intensity of each NP in the L matrix for each pixel of an image. L_{ji} is the scattering intensity, $I_i(j + 449)$, of the i^{th} NP at the j^{th} channel (wavelength, $\lambda = j + 449$ nm, ranging from 450 to 700 nm, totally m of 251 channels). For example, L_{11}, L_{21}, …L_{m1} represents the scattering intensity of the LSPR spectrum of the 1st NP, and L_{1n}, L_{2n}, …L_{mn} represents the scattering intensity of the LSPR spectrum of the n^{th} NP.

Note that w_i is the percent of scattering intensity of i^{th} NPs in the total scattering intensity contributed by total number (n) of NPs in each pixel, as described in eqn (6):

$$I_{i,x,y}(\lambda) = w_i I_{x,y}(\lambda) \quad (6)$$

where $I_{i,x,y}(\lambda)$ is the scattering intensity of the i^{th} NPs at a given wavelength (λ) in a pixel located in (x, y) of a CCD pixel array. $I_{x,y}(\lambda)$ is the total scattering intensity of n NPs (undeconvoluted NP cluster) at the same given wavelength in the same pixel. Thus, sum of w_i is equal to one.

The least squares approximation is used to minimize the residuals (e) and to obtain the best values of $\boldsymbol{w}$, as described below in eqn (7):

$$e = \|L\boldsymbol{w} - \boldsymbol{S}_{x,y}\|^2 \quad (7)$$

After deconvolution (un-mixing) of each image cube, a gray-scale image in TIFF format for each NP (SMNOBS) with a given LSPR spectrum was generated. The image was then fitted by PSF using 2D-Gaussian distribution (Fig. S5B and S7B†), as described below in eqn (8):[40,55]

$$N_{x,y} = B + N_{00} e^{-\frac{1}{2}\left[\left(\frac{x-x_0}{S_x}\right)^2 + \left(\frac{y-y_0}{S_y}\right)^2\right]} \quad (8)$$

where (x_0, y_0) is the centroid of the scattering point; $N_{x,y}$ is the scattering intensity of a NP at the pixel (x, y); N_{00} is the scattering intensity at the centroid (x_0, y_0); S_x and S_y are the widths of the PSF in x and y directions, respectively; and B is the background intensity.

The center position of the 2D-Gaussian fitting is the precise location (centroid) of each NP. The standard deviation (SD) of the centroid is determined using FWHM of the 2D-Gaussian fitting curve, as described below in eqn (9):

$$\mathrm{SD} = \frac{\mathrm{FWHM}}{2\sqrt{2\ln 2}} \approx \frac{\mathrm{FWHM}}{2.355} \quad (9)$$

Using the same approaches, 20 image cubes are taken and 20 precise locations for each NP are analyzed, as described above (Fig. S5A and S7A†). The 20 precise locations of each NP are then fitted by 2D-Gaussian, as described by eqn (8) (Fig. S5BC and S7BC†). The peak position of the 2D-Gaussian fitting curve for 20 precise locations of each NP is used to determine the

precise location of each SMNOBS bound with single TNFR1 molecules (single L–R complexes) on/in single live cells. Standard deviation of the precise location of each NP is determined using FWHM of the 2D-Gaussian fitting curve, as described by eqn (9).

By locating the precise positions of single SMNOBS bound with their receptors on/in single live cells in real-time, the number of individual L–R complexes in selected detection volume (areas) on/in single cells is determined over time (Fig. 6–10).

Data analysis and statistics

A minimal of 300 single NPs (Ag, AgMMUA, and AgMMUA–TNFα NPs) were characterized to determine their sizes and shapes using HRTEM, and their plasmonic properties (images and LSPR spectra) using DFOMS, with a minimal of 100 single NPs for each of three replicated experiments. More than 10 individual cells incubated with either the cell culture medium, TNFα, AgMMUA NPs, or AgMMUA–TNFα NPs, were imaged simultaneously over time using PHOTON and fluorescence microscopy. For three replicated experiments, 26–30 individual cells for each study and each control experiment were characterized to gain sufficient statistics to study molecular mechanisms and kinetics of TNFα-induced apoptosis pathways of bulk cells at the single-cell resolution.

Acknowledgements

This work is supported in part by NSF (NIRT: CBET 0507036) and NIH (R01 GM076440; 3R01 GM 76440-01S1; and 3R01 GM076440-045). Browning is grateful for the support of NIH-GRAS (R01 3GM0764401-S) and an Old Dominion University Fellowship.

References

1 H. Wajant, K. Pfizenmaier and P. Scheurich, *Cell Death Differ.*, 2003, **10**, 45–65.
2 G. M. Delgoffe, P. J. Murray and D. A. Vignali, *Curr. Opin. Immunol.*, 2011, **23**, 623–638.
3 I. Bethani, S. S. Skånland, I. Dikic and A. Acker-Palmer, *EMBO J.*, 2010, **29**, 2677–2688.
4 F. Van Herreweghe, N. Festjens, W. Declercq and P. Vandenabeele, *Cell. Mol. Life Sci.*, 2010, **67**, 1567–1579.
5 M. E. Guicciardi and G. J. Gores, *FASEB J.*, 2009, **23**, 1625–1637.
6 C. F. Bohren and D. R. Huffman, in *Absorption and Scattering of Light by Small Particles*, Wiley, New York, 1983, pp. 287–380.
7 K. L. Kelly, E. Coronado, L. L. Zhao and G. C. Schatz, *J. Phys. Chem. B*, 2003, **107**, 668–677.
8 U. Kreibig and M. Vollmer, in *Optical Properties of Metal Clusters*, Springer, Berlin, 1995, pp. 14–123.
9 G. Mie, *Ann. Phys.*, 1908, **25**, 377–445.
10 P. D. Nallathamby, T. Huang and X.-H. N. Xu, *Nanoscale*, 2010, **2**, 1715–1722.
11 T. Huang, P. D. Nallathamby and X.-H. N. Xu, *J. Am. Chem. Soc.*, 2008, **130**, 17095–17105.
12 T. Huang and X.-H. N. Xu, *Nanoscale*, 2011, **3**, 3567–3572.
13 P. D. Nallathamby, K. J. Lee and X.-H. N. Xu, *ACS Nano*, 2008, **2**, 1371–1380.
14 T. Huang, P. D. Nallathamby, D. Gillet and X.-H. N. Xu, *Anal. Chem.*, 2007, **79**, 7708–7718.
15 K. J. Lee, L. M. Browning, T. Huang, F. Ding, P. D. Nallathamby and X.-H. N. Xu, *Anal. Bioanal. Chem.*, 2010, **397**, 3317–3328.
16 K. J. Lee, P. D. Nallathamby, L. M. Browning, C. J. Osgood and X.-H. N. Xu, *ACS Nano*, 2007, **1**, 133–143.
17 P. D. Nallathamby, K. J. Lee, T. Desai and X.-H. N. Xu, *Biochemistry*, 2010, **49**, 5942–5953.
18 X.-H. N. Xu, W. J. Brownlow, S. V. Kyriacou, Q. Wan and J. J. Viola, *Biochemistry*, 2004, **43**, 10400–10413.
19 X.-H. N. Xu, J. Chen, R. B. Jeffers and S. V. Kyriacou, *Nano Lett.*, 2002, **2**, 175–182.
20 J. Lippincott-Schwartz and S. Manley, *Nat. Methods*, 2009, **6**, 21–23.
21 R. Y. Tsien and A. Waggoner, in *Handbook of Biological Confocal Microscopy* ed. J. B. Pawley, Plenum, New York, 2nd edn, 1995, pp. 267–280.
22 R. M. Locksley, N. Killeen and M. J. Lenardo, *Cell*, 2001, **104**, 487–501.
23 K. J. Tracey, *Nature*, 2002, **420**, 853–859.
24 C. Haworth, R. N. Maini and M. Feldman, in *The Cytokine Handbook*, ed. A. Thomson, Academic Press, 1998, pp. 777–801.
25 S. W. Lowe, E. Cepero and G. Evan, *Nature*, 2004, **432**, 307–315.
26 M. Tagawa, *Curr. Pharm. Des.*, 2000, **6**, 681–699.
27 O. Micheau and J. Tschopp, *Cell*, 2003, **114**, 181–190.
28 L. A. Tartaglia, R. F. Weber, I. S. Figari, C. Reynolds, M. A. Palladino, Jr and D. V. Goeddel, *Proc. Natl. Acad. Sci. U. S. A.*, 1991, **88**, 9292–9296.
29 N. L. Vujanovic, *Immunol. Res.*, 2011, **50**, 159–174.
30 J. Muntané, *Chem. Res. Toxicol.*, 2011, **24**, 1610–1616.
31 T. J. Sayers, *Cancer Immunol. Immunother.*, 2011, **60**, 1173–1180.
32 H. Hövel, S. Fritz, A. Hilger, U. Kreibig and M. Vollmer, *Phys. Rev. B: Condens. Matter*, 1993, **48**, 18178–18188.
33 F. Hubenthal, *Prog. Surf. Sci.*, 2007, **82**, 378–387.
34 K. Nagahira, Y. Fukuda, M. Terakawa, J. Hashino, T. Nasu, H. Nakazato and T. Nakanishi, *Immunol. Lett.*, 1995, **46**, 135–141.
35 A. Moller, F. Emling, D. Blohm, E. Schlick and K. Schollmeier, *Cytokine*, 1990, **2**, 162–169.
36 B. W. Lee, G. L. Johnson, S. A. Hed, Z. Darzynkiewicz, J. W. Talhouk and S. Mehrotra, *BioTechniques*, 2003, **35**, 1080–1085.
37 S. Elmore, *Toxicol. Pathol.*, 2007, **35**, 495–516.
38 V. D. Barnett, *J. Am. Stat. Assoc.*, 1966, **61**, 1205–1218.
39 A. Delaigle, P. Hall and A. Meister, *Ann. Stat.*, 2008, **36**, 665–685.
40 R. E. Thompson, D. R. Larson and W. W. Webb, *Biophys. J.*, 2002, **82**, 2775–2783.
41 M. C. DeSantis, S. H. DeCenzo, J. L. Li and Y. M. Wang, *Opt. Express*, 2010, **18**, 6563–6576.
42 H. Qian, M. P. Sheetz and E. L. Elson, *Biophys. J.*, 1991, **60**, 910–921.
43 A. Kusumi and Y. Sako, *J. Cell Biol.*, 1994, **125**, 1251–1264.
44 A. Kusumi, Y. Sako and M. Yamamoto, *Biophys. J.*, 1993, **65**, 2021–2040.
45 L. M. Browning, K. J. Lee, T. Huang, P. D. Nallathamby, J. Lowman and X.-H. N. Xu, *Nanoscale*, 2009, **1**, 138–152.
46 W. R. Dunham, R. H. Sands, S. B. Klein, E. A. Duell, L. M. Rhodes and C. L. Marcelo, *Spectrochim. Acta, Part A*, 1996, **52**, 1357–1368.
47 A. M. Mastro, M. A. Babich, W. D. Taylor and A. D. Keith, *Proc. Natl. Acad. Sci. U. S. A.*, 1984, **81**, 3414–3418.
48 T. Huang and X.-H. N. Xu, *J. Mater. Chem.*, 2010, **20**, 9867–9876.
49 X.-H. N. Xu, S. Huang, W. Brownlow, K. Salatia and R. Jeffers, *J. Phys. Chem. B*, 2004, **108**, 15543–15551.
50 P. D. Nallathamby and X.-H. N. Xu, *Nanoscale*, 2010, **2**, 942–952.
51 S. C. Gebhart, R. C. Thompson and A. Mahadevan-Jansen, *Appl. Opt.*, 2007, **46**, 1896–1910.
52 R. D. B. Fraser and E. Suzuki, *Anal. Chem.*, 1969, **41**, 37–39.
53 T. Klar, M. Perner, S. Grosse, G. von Plessen, W. Spirkl and J. Feldmann, *Phys. Rev. Lett.*, 1998, **80**, 4249–4252.
54 D. L. Farkas, C. Du, G. W. Fisher, C. Lau, W. Niu, E. S. Wachman and R. M. Levenson, *Comput. Med. Imaging Graphics*, 1998, **22**, 89–102.
55 X. Qu, D. Wu, L. Mets and N. F. Scherer, *Proc. Natl. Acad. Sci. U. S. A.*, 2004, **101**, 11298–11303.

Published on 04 January 2012 on http://pubs.rsc.org | doi:10.1039/C2NR11739H
Downloaded by Old Dominion University on 18 April 2012

 This journal is © The Royal Society of Chemistry 2012